MODELING HIV-1 INFECTION IN THE BRAIN: THE EFFECT OF THE BLOOD-BRAIN BARRIER

A DISSERTATION IN
Mathematics
and
Physics

Presented to the Faculty of the University
of Missouri-Kansas City in partial fulfillment of
the requirements for the degree

DOCTOR OF PHILOSOPHY

by
COLIN T. BARKER

B.A., Drury University, Springfield, Missouri, 2011
M.S., University of Missouri-Kansas City, 2015

Kansas City, Missouri
2020

MODELING HIV-1 INFECTION IN THE BRAIN: THE EFFECT OF THE BLOOD-BRAIN BARRIER

Colin T. Barker, Candidate for the Doctor of Philosophy Degree

University of Missouri-Kansas City, 2020

ABSTRACT

Despite the advancement of antiretroviral therapy (ART), the development of HIV associated neurocognitive disorders (HAND) remains a major concern among HIV infected patients. As many ART drugs may fail to penetrate the blood-brain barrier (BBB), the long-term presence of viral RNA in the brain is considered to be associated with these disorders, such as early-onset dementia. *In vivo* study of HIV infection in the brain is extremely difficult, and thus mathematical modeling can help to further the analysis of the viral dynamics of HIV in the brain. In this dissertation we develop a mathematical model to help investigate the viral dynamics of HIV in the brain. Our model can explain containing viral loads in the plasma and in the cerebral spinal fluid from SIV-infected macaques. We then extend this model to study the treatment of HIV in the brain. Furthermore we develop a new stochastic model to analyze any stochastic effects that may underlie HIV-viral dynamics in the brain. Using our models, we show that the rate of transport of infected macrophages

into the brain greatly exceeds the rate of transport out of the brain. We also show that viral replication occurs in the brain, suggesting that the brain can act as a viral reservoir. We also show that the basic reproduction number largely depends on the overall effectiveness of ART, but it is not strongly affected by the rate of drug penetration through the blood-brain barrier. The effectiveness of ART depends on both pharmacodynamic parameters and a drug's ability to penetrate through the BBB. In particular, for drugs with a high dose-response curve, the BBB penetration strongly affects the post-treatment control of the virus in the brain. Through examination of the stochastic model we illustrate a prolonged higher likelihood of infection and viral production in the brain compared to the plasma. Results in this dissertation may be useful to develop HIV control strategies to target the virus hiding in the brain.

The faculty listed below, appointed by the Dean of the School of Graduate Studies, have examined a dissertation titled "Modeling HIV-1 Infection in the Brain: The Effect of the Blood-Brain Barrier", presented by Colin T. Barker, candidate for the Doctor of Philosophy degree, and certify that in their opinion it is worthy of acceptance.

Supervisory Committee

Naveen Vaidya, Ph.D., Committee Chair
Department of Mathematics and Statistics, San Diego State University

Noah Rhee, Ph.D.
Department of Mathematics and Statistics

Xianping Li, Ph.D.
Department of Mathematics and Statistics

Anthony Caruso, Ph.D.
Department of Physics and Astronomy

Youan Bi-Botti, Ph.D.
UMKC School of Pharmacy

CONTENTS

ILLUSTRATIONS

TABLES

ACKNOWLEDGMENTS

First, I would like to thank my advisor, Dr. Naveen Vaidya, for his time, patience, encouragement, and tireless guidance. I am very appreciative of the support he has provided me over the last few years.

Second, I would like to recognize my committee, Dr. Noah Rhee, Dr. Xianping Li, Dr. Anthony Caruso, and Dr. Youan Bi-Botti for their guidance.

In addition to my committee, I would like to thank Dr. Feng-Bin Wang for his insights and aid on the theoretical aspects of global analysis. And I wish to thank Dr. Liana Sega, Dr. Eric Hall, Dr. Majid Bani-Yaghoub, Dr. Anil Kumar, and my friend, office mate, and constant source of encouragement, Jones Mutua.

Finally, I want to thank my wife, Whitney, for her undying support, and for tolerating my seemingly Sisyphean pursuit of this degree.

CHAPTER 1

INTRODUCTION

Human immunodeficiency virus (HIV-1) is one of the most deadly diseases in the world. According to the CDC [4] roughly 37 million people currently live in the world with the disease, including 1.8 million new cases in 2017. In 2017, nearly one million people died of HIV-1 globally. Restricting this to the United States the numbers remain staggering, with roughly 1.1 million people in the United States currently live with the disease, and nearly 40,000 new infections occurred in the year 2017.

Typically HIV-1 is transmitted between individuals via sexual intercourse or via syringe and needle use. Transmission only occurs if contaminated blood (or fluids such as breast milk, semen, pre-seminal fluid, rectal, and vaginal fluids) comes into contact with damaged skin or is directly injected into the bloodstream. Once entered into the system HIV-1 spreads rapidly throughout the body and eventually may lead to Acquired Immunodeficiency Syndrome (AIDS) [4]. HIV-1 (Figure 1) in the form of AIDS attacks and weakens the immune system and then may lead to opportunistic infection of other diseases. Current treatment has progressed enough to allow infected individuals to maintain an almost full lifespan with HIV-1, however no cure has yet been found, despite potential recent success via stem-cell transplants [49]. Because no cure exists, several studies explore methods to optimally control the virus.

A major barrier in the efforts to treat HIV-1 is the existence of viral reservoirs

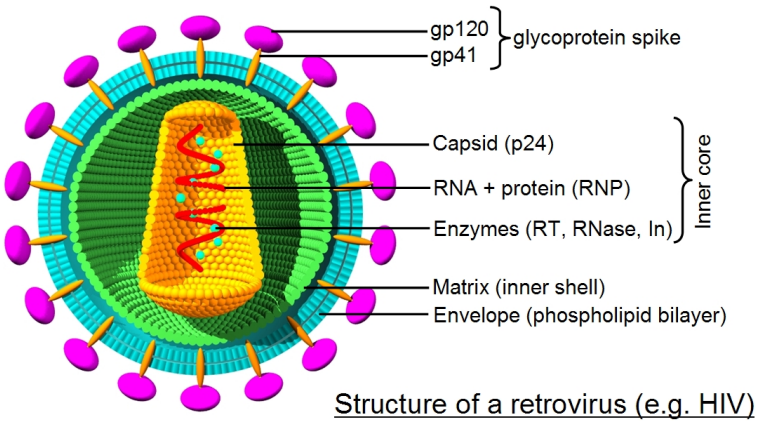

Figure 1: Structure of an HIV virion [3].

in many sites such as the gut, liver, reproductive organs, and the brain [24, 27]. HIV DNA resides latently within a reservoir, develops into virus particles and then leaks into the plasma and reinfects the bloodstream. While each reservoir merits significant research, the brain is the least studied reservoir. This is partly because *in vivo* study is difficult and expensive, often requiring a spinal tap. As the lifespans of HIV-1 infected individuals has increased, the long-term virus within the brain often leads to HIV-1 associated neurocognitive diseases (HAND) such as early-onset dementia and encephalitis [18, 41, 43, 50, 51, 59]. It is thus critical to understand the viral dynamics of HIV-1 in the brain.

HIV-1 enters the brain by crossing the blood-brain barrier (BBB) which facilitates transport of cells between the bloodstream and the brain [9, 12, 53]. Unfortunately, antiretroviral drugs fail to pass through the BBB with the same effectiveness, allowing the virus to persist in the brain despite ongoing treatment [46]. The virus

then leaks out [13] again through the BBB back into the bloodstream and produces more infection throughout the body. Hence, to study the viral dynamics of HIV-1 in the brain it is paramount to consider the role of the BBB on viral transport.

Although some drugs may struggle to pass through the BBB, the treatment of HIV-1 still plays a vital role in the control of HIV-1. Several types of drug mechanisms exist whose combinations make up what is called highly-active antiretroviral therapy (HAART). The drugs target inhibiting some stage of the life-cycle of the virus. Multiple studies [46, 48, 57, 63, 74, 75, 60] offer insight into the mechanisms of these drugs and their overall effectiveness on HIV-1 control. A study by Letendre [46], measured the permeability of commonly prescribed ART drugs through the BBB and found that there are only a few drugs that show a stronger ability to pass through the BBB. While these drugs often control the virus despite failing to eradicate it from the system, they are crucial to the evaluation of HIV-1 in the brain.

Mathematical modeling has proven to be a useful tool to aid our understanding of the viral dynamics of HIV-1 [14, 32, 34, 40, 56, 57]. However, limited studies have been done which include the brain or the BBB. The goal of this dissertation is to develop mathematical models that offer insights into the effects of the BBB on the viral dynamics of HIV-1 in the brain, and on the effectiveness of treatment to control the virus in the brain.

The dissertation is organized in as follows: In Chapter 2 we provide relevant background for modeling HIV-1 dynamics as well as important biological information about HIV-1, the BBB, and antiretroviral therapy. We also present various techniques for theoretical analysis used in this dissertation.

In Chapter 3 we develop a nonlinear ordinary differential equation (ODE) model to study the role of the BBB on the viral dynamics of HIV-1 in the brain. The model is parameterized using viral load data from macaques infected with a mixture of simian-immunodeficiency virus (SIV) and simian-human-immunodeficiency virus (SHIV). We conduct a thorough sensitivity analysis of the model parameters.

In Chapter 4 we develop and analyze an ODE model to examine the effect of the BBB on the effectiveness of treatment to control HIV-1 in the brain. We also conduct global stability analysis of the model. Furthermore, we examine the effect of the drug pharmacodynamics, as well as the drug permeability through the BBB, on the viral dynamics of HIV1.

In Chapter 5 we develop a stochastic differential equations (SDE) model to study the impact of the stochastic nature of the virus-cell dynamical system. We compare the simulations of the SDE model with the ODE model and analyze important state probability distributions and likelihoods of infection events.

Finally, in Chapter 6 we discuss important findings of our study, biological implications and future directions. We also present the conclusion of the dissertation.

CHAPTER 2

BACKGROUND INFORMATION

In this chapter we provide a brief literature review of the biological aspects of HIV as well as of relevant mathematical modeling for HIV viral dynamics. We also detail some of the methods used in the theoretical analysis of the models developed in this dissertation.

HIV Life Cycle

In order for HIV to spread, a free HIV virion must infect a cell. The most common target cells are white blood cells known as helper T cells, specifically CD4+ T cells [2]. These cells play a major role in the immune system which fights against infection within the body. Typically CD4+ T cells recognize foreign substances within the body through coreceptors like CCR5 or CXCR4. A free HIV virion attaches to a CD4+ T cell by binding to these coreceptors. After binding, the viral envelope fuses with the cell and the viral RNA enters the CD4+ T cell and releases enzymes to begin viral reproduction. The first enzyme, reverse transcriptase, allows the virus to convert HIV RNA into HIV DNA, thus allowing HIV to enter the nucleus of the CD4+ T cell. The second enzyme, integrase, allows the HIV DNA to insert itself into the DNA of the T cell, and through the normal mitosis process of the T cell, viral HIV DNA is then replicated. Since HIV is a retrovirus, these replications may not be exact. As long chains of the HIV RNA are created by this process, they assemble outside of the nucleus and move toward the surface of the cell. HIV is still non-infectious at

this stage. The final stage, known as budding, occurs when the newly formed HIV releases the enzyme protease to break up the long RNA protein chains of HIV into smaller HIV RNA proteins, which bud off of the CD4+ T cell, and release into the body [2]. A diagram of this process is provided in Figure 2.

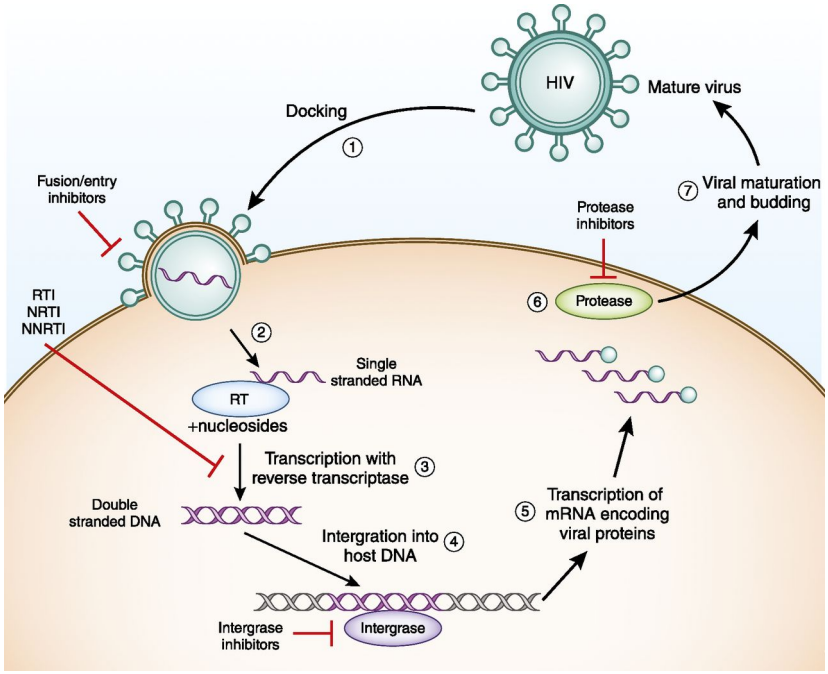

Figure 2: The seven stages of the HIV life cycle [10]

An individual infected by HIV experiences two stages of infection before developing Acquired Immunodeficiency Syndrome (AIDS): acute infection and chronic infection. During acute infection the viral load of HIV spikes, then dips to a consistent (chronic) lower level that can maintain for several years. An individual may express flu-like symptoms during acute infection.

A CD4+ T cell is not the only target cell for HIV infection. Another cell, known as a macrophage, is also commonly utilized for viral replication. This was first discovered in 1986 by Koenig *et al* [41]. The infection process within macrophages is similar to that of a CD4+ T cell, although the lifespan of a macrophage is much longer than that of a CD4+ T cell [53]. Notably macrophages can enter into the brain (the cerebral spinal fluid, or CSF), whereas a CD4+ T cell typically remains within the plasma.

HIV Control and Treatment

In an effort to control the HIV replication process, HIV antiretroviral drugs have been developed. These drugs are classified based on the part of the HIV life cycle they disrupt. Specifically, the classes of HIV drugs are fusion inhibitors (FIs), reverse transcriptase inhibitors (these are subclassified as non-nucleotide reverse transcriptase inhibitors, NRTIs, and nucleotide reverse transcriptase inhibitors, NNRTIs, respectively), integrase inhibitors (IIs), and protease inhibitors (PIs). The stage of the HIV life-cycle that each class of drug inhibits is also marked in Figure 2. Treatment plans including any combination of drugs were previously known as highly-active antiretroviral therapy (HAART), although they are more commonly referred to simply as antiretroviral therapy (ART).

ART treatments currently control HIV well enough such that an infected individual currently undergoing ART may live to a normal lifespan. Long-term infection of HIV has been shown to lead to nuerocognitive disorders like early-onset dementia and encephalitis [42]. These chronic diseases are referred to as HIV-associated neurocognitive disorders (HAND), and are currently an important area of study.

Viral Reservoirs

After interruption of ART, HIV-infected individuals experience a rebound of the virus. This is largely due to latent reservoirs of HIV [54]. A viral reservoir is a site within the body which harbors viral RNA. Since the latently infected cells do not produce virus at the current stage, ART fails to clear the virus from these reservoirs, which allows for later activation after ART is withdrawn. Common HIV viral reservoirs are the gut, liver, reproductive organs, and the brain [24, 31, 27].

The Brain and the BBB

Although CD4+ T cells rarely enter the brain, viral RNA copies have been observed in the cerebral-spinal fluid (CSF) in as early as one week post-infection [35, 51]. The CD4+ T cells fail to enter the brain due to the presence of the blood-brain barrier (BBB). The BBB consists of a variety of endothelial cells, macrophages, and astrocytes (see Figure 3), and mitigates transit of cells between the cerebral-spinal fluid and the bloodstream by phosphorylation initiated by polarization [35]. Not only does the BBB prevent most CD4+ T cells from entering into the brain, but also there is little evidence to suggest that free HIV-1 virions can pass through the BBB. Instead, the virus infects immature macrophages (known as monocytes) which take advantage of macrophage turnover within the BBB, and thus enter the brain. This method is commonly referred to as the "Trojan-horse" method.

The BBB is a unique feature among the viral reservoirs of HIV, as productive (rather than latent) free virions exist inside the CSF and reside even throughout ongoing ART. It is not well understood how HIV acts within the brain, as *in vivo* study is difficult. A study by Letendre *et al.* [46] provided a measure for the effectiveness of

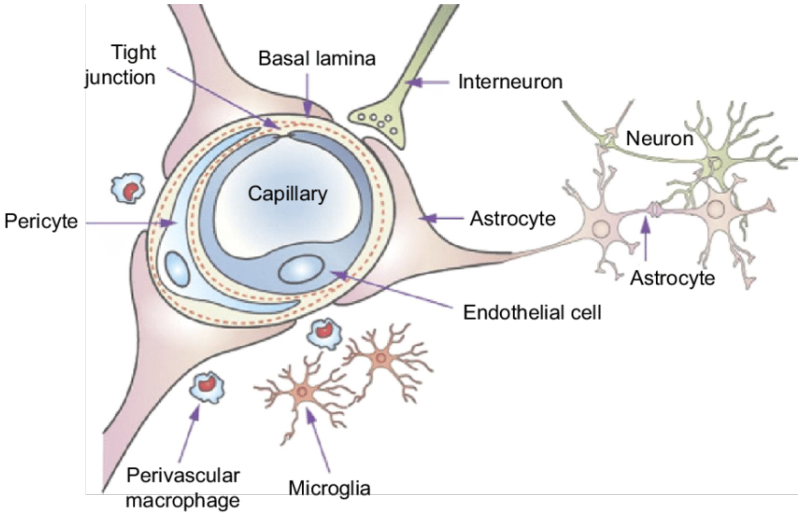

Figure 3: Schematic diagram of the blood-brain barrier [5]

ART drugs to permeate the BBB. Given the important role of the BBB on the virus and drug entry, understanding the effect of the BBB on the viral dynamics of HIV and ART is thus very important.

Viral Dynamics Modeling with a Deterministic Approach

In this section, we present a brief summary of articles that focus on within-host HIV infection modeling, paying special attention to those related to viral reservoirs and the brain. We also highlight a few experimental studies that are useful to developing models.

A deterministic viral dynamics model uses a system of ordinary differential equations (ODE) that may or may not depend upon each other to represent incremental rates of change. These rates are captured by model parameters and have been widely useful in understanding natural phenomena.

Some of the earliest deterministic models of HIV viral dynamics [40, 78] include three compartments of cells: uninfected CD4+ T cells, T, infected CD4+ T cells, I, and free HIV virions, V (Figure 4).

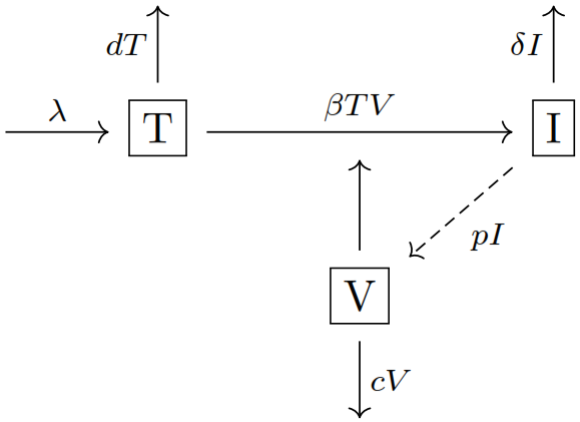

Figure 4: The schematic diagram of the basic model of HIV-1 infection.

In this model the CD4+ T cells are generated at a constant rate λ, and die at a per capita rate of d. Uninfected target cells become infected at a rate β when they interact with free virions. These infected cells produce new virions at a rate of p per infected cell. Infected cells die at a per capita rate δ. Free virions get cleared at a constant per capita rate of c. Mathematically this model can be described by the following system of ordinary differential equations (ODEs):

$$\begin{aligned}
\frac{\mathrm{d}T}{\mathrm{d}t} &= \lambda - \beta VT - dT, \\
\frac{\mathrm{d}I}{\mathrm{d}t} &= \beta VT - \delta I, \\
\frac{\mathrm{d}V}{\mathrm{d}t} &= pI - cV.
\end{aligned} \tag{2.1}$$

This simple model showed remarkable success at describing the dynamics of acute HIV infection [32, 57] and initiated the emergence of the field of study of viral dynamics [55, 73].

Callaway and Perelson [14] extended the basic model (2.1) to consider two infection compartments. This allowed them to study chronically infected cells, quiescent cells, latently infected cells, and even treatment. These models provided insight into identifying populations of drug-resistant cells, and low steady-state viral loads. In particular, from these models it was observed that target cells can respond differently to ART drugs. A major question from this study was whether drugs could be developed to cross physiological barriers better, in the hopes of completely eradicating HIV-1 from the human body.

Kim and Perelson [39] created a mathematical model of latent viral reservoirs. This model describes the stability and decay characteristics of a latent reservoir. They were able to model the "extremely slow decay" and stability of the latent reservoir due to ongoing viral replication together with what they called bystander proliferation. That is, nonstandard virus proliferation, for example, proliferation due to cytokines in the environment. Their results suggest that even amid ongoing ART, low-level viremia exists untreated within latent reservoirs. An excellent reference for further review on mathematical models of latent HIV-1 infection can be found in Rong and

Perelson [57].

The previous models were very effective in describing viral reservoirs, but declined to specify the type of reservoir. The BBB's unique mechanism for preventing treatment has had very little study by mathematical modeling. Recently Roda *et al.* [56] developed a model to explore specifically the viral dynamics within the brain. They used a simple model with only two compartments–uninfected and infected macrophages. The results of the model suggest that the virus in the brain can be eradicated depending on the comorbidity in the brain and the macrophage lifespan.

Shortly after Roda *et al.* [56] published their study, another study by Huang *et al.* [34] developed a model to analyze HIV persistence with regards to the lymphocyte recirculation network within the CNS. The numerical results of their study illustrated that plasma viral load data may not accurately reflect the overall viral mechanisms of HIV within the human body. More research is clearly needed about HIV in the brain.

Data Fitting

For a given system of Ordinary Differential Equations (ODEs), unknown parameters can be estimated by fitting a model solution to data. Throughout this dissertation the ODEs presented are solved numerically using the MATLAB solvers "ode15s" and "ode45". For data fitting, the optimization functions "fmincon" and "fminsearch" are used along with the common technique of the least squares method. This method minimizes the sum of the squared residuals, that is, the difference between model predictions and their corresponding experimental data values. The for-

mula below calculates the sum of the squared residuals.

$$J = \frac{1}{M}\sum_{i=1}^{M}(y - y_i)^2 \tag{2.2}$$

Here M represents the total number of data points considered for fitting and y and y_i represent the values predicted by the model and those from the experimental data, respectively.

Once the best model parameters are computed from the least squares method, it is common to further evaluate these parameters by finding confidence intervals (CIs). CIs are calculated from n replications via bootstrapping the residuals from the formula (2.2) [11, 23]. We note that this bootstrap method uses sampling with replacement, so randomly selected data points may be repeated.

The process for generating CIs for estimated parameters by the bootstrapping method is given as follows:

1) Select a sample of m data points;
2) Re-sample the m data points several times with replacement;
3) Perform a model simulation and calculate the residual error between the simulated solution and the data point for each data point;
4) From the residual errors in the previous step compute their standard deviation, σ;
5) For each data point add a randomly chosen error term to each simulated solution at that point and call it the new data point. The error is chosen from a normal distribution with standard deviation σ.
6) Repeat the previous four steps n times;

7) Run the model simulations using each of the n bootstrapped data points;

8) Calculate 95% confidence intervals based off the results of these simulations.

Model Comparison

A well-known method to compare the quality of mathematical models relative to each other is to use the Akaike Information Criterion (AIC). By comparing computed AIC values, a model is chosen by taking the lowest AIC value calculated among all models. The AIC is computed using the following formula [6]

$$\text{AIC} = P \ln\left(\frac{J}{P}\right) + \frac{2P(N_p+1)}{P-N_p-2}, \tag{2.3}$$

where J is the sum of the squared residuals from formula (2.2), P is the number of data points used to fit the model, and N_p is the number of parameters estimated for the fitting. Note that $\ln(x)$ is meant as the logarithm of x with the natural base e.

The Basic Reproduction Number $\mathfrak{R}_0$

For within-host models, a critical number that is highly analyzed is the basic reproduction number, $\mathfrak{R}_0$. $\mathfrak{R}_0$ represents the average number of secondary infections arising from a single infected cell residing within entirely uninfected cells [22]. The most common method to compute $\mathfrak{R}_0$ is the next-generation operator method [22]. In this method, we consider the equations related to infectious terms compartments and linearize them about the infection-free equilibrium. Then we introduce two matrices, the first matrix, denoted F, containing infection terms and the second matrix, V, containing the transfer terms. The total new infections can be thus represented by the product, FV^{-1}. The basic reproduction number $\mathfrak{R}_0$ is then taken to be the

largest eigenvalue of FV^{-1}. In mathematical notation we consider the two matrices $F = \left[\frac{\partial F_i(x_0)}{\partial x_j}\right]$, and $V = \left[\frac{\partial V_i(x_0)}{\partial x_j}\right]$, where F_i represents the new infections and V_i represents the transfer terms. The value x_0 represents the infection-free equilibrium and the basic reproduction number, $\mathfrak{R}_0$, is the spectral radius given by $\rho(FV^{-1})$.

Equilibria, Bifurcation Analysis, and Stability

Mathematical models are most useful in their ability to model and predict natural behavior and phenomena. Naturally, understanding the stability of system solutions is necessary to validate the use of such a model. For a deterministic ODE model an equilibrium solution is a model solution such that each derivative does not change. This solution can be determined by setting all derivatives equal to zero. In viral dynamics modeling, it is common to determine the infection-free equilibrium (IFE). Moreover, equilibria may be stable or unstable depending on several features of the system. While there are numerous methods to determine stability, one used in this dissertation is the application of Lyapunov function. Utilizing Lyapunov's second method of stability [26] if one can find a Lyapunov function $L : \mathbb{R}^n \to \mathbb{R}$, defined to be a scalar function such that 1) $L(\mathbf{x}) = 0$ if and only if $\mathbf{x} = 0$, 2) $L(\mathbf{x}) > 0$ if and only if $\mathbf{x} \neq 0$, and 3) $\frac{\mathrm{d}L(\mathbf{x})}{\mathrm{d}t} < 0$ for all $\mathbf{x} \neq 0$, then the equilibrium point $\mathbf{x}_0$ is asymptotically stable, where $\mathbf{x}$ is the ODE system.

It may be the case that a single solution approaches an equilibrium point under one set of conditions, yet under different conditions it may tend away from an equilibrium point. The point in which the solution changes is commonly referred to as a bifurcation point. Often in disease modeling the basic reproduction number $\mathfrak{R}_0$ helps determine such bifurcations. In particular, if the system parameters yield

a solution that does not tend toward the infection-free equilibrium, by analyzing the bifurcation it may be determined that viral infection persists.

Viral Dynamics Modeling with a Stochastic Approach

All modeling techniques so far have been deterministic by nature, but many events including cell-to-cell interaction tends to occur with a degree of randomness and uncertainty. Models using systems of stochastic differential equations (SDEs) help capture this randomness by including a term of Brownian motion.

While many deterministic models have been developed to analyze HIV viral dynamics, there have been far fewer stochastic models. An SDE population dynamic model by Tuckwell *et al.* [72] used uninfected cells, infected cells, latently infected cells, and viral particles to model early HIV infection. Another study by Tan *et al.* [69] examined stochastic effects on HIV viral dynamics using Monte Carlo methods.

There are several methods to create SDE models [80, 7, 25], but in this dissertation we use a method developed by Cao and Gillespie [15]. This method is known as the τ-leap method, which approximates a stochastic simulation algorithm (SSA) by predicting common events and skipping over time differentials, or τs. This differs from the method proposed by Gillespie [25] in several ways, for example, the normal random variables in the Gillespie SSA become Poisson random variables in the τ-leap method.

A viral dynamics model using an SDE can be derived based upon the ODE model from system (2.1). We now present an outline of the method. First we determine the number of possible events that could occur in a small time interval and represent each event with a vector of the state changes for each compartment. For

example, if the states of each compartment are represented by $\vec{\mathbf{X}} = [T, I, V]^{\mathrm{tr}}$, then the vector $\vec{\mathbf{X}} = [-1, 1, -1]^{\mathrm{tr}}$ represents the event that a single target cell becomes infected. In this case of the basic $[T, I, V]$ model there are seven possible events, including the event $\vec{\mathbf{X}} = [0, 0, 0]^{\mathrm{tr}}$, in which no change occurs. We then assign a probability to each event determined by the model. For example, the uninfected T-cell reaction $\vec{\mathbf{X}}$ has a probability of $p = dT$. Note that the probability in this case is identical to the rate from the deterministic model, although this is not generally the case. The probability that no change occurs is simply the complement of the sum of all events in which a state change takes place. The choice of which event occurs in a given time interval depends on the probability of each event.

CHAPTER 3

MODELING THE ROLE OF THE BBB ON THE HIV DYNAMICS IN THE BRAIN

In this chapter we develop a novel mathematical model to describe the HIV-1 viral dynamics in the brain. We identify key parameters by fitting our model to plasma and CSF viral load data from an experiment using rhesus macaques infected with a mixture of Simian Immunodeficiency Virus (SIV) and Simian-Human Immunodeficiency Virus (SHIV). We consider three variants of the model to analyze viral replication within the brain. We also explore the long-term stability of HIV-1 predicted by our model and determine its sensitivity to key parameters.

Introduction

The long-term effects of HIV-1 in the brain are devastating. Despite undetected viral load in the plasma during HAART, many patients experience HIV associated neurocognitive disorders (HAND), such as encephalitis and early-onset dementia [41, 46, 48, 63], mostly due to the extended period of infected individuals carrying the virus supplied from the reservoirs. Among the viral reservoirs the brain represents the least studied one [12, 13, 18, 24, 27, 46, 50], because of its unique feature associated with the blood-brain barrier (BBB) and the difficulty of *in vivo* study on the brain infection. It is important to get insights into the viral dynamics in the brain to devise proper HIV-1 control strategies.

Recent studies have considered the virus in the brain as a major obstacle in

the search for a cure [24, 31]. The brain has been recognized as a viral reservoir, but it still remains unclear whether or not viral replication occurs within the brain [27, 48, 57, 59, 63]. Some effort has been made to suppress the virus within the brain, but the BBB drastically reduces the effectiveness of such treatment, partly because many drugs cannot cross the BBB [9, 46]. Due to the difficulty in controlling HIV-1 in the brain as well as potential viral replication inside it, the brain can be an important reservoir causing an obstacle for a cure [12, 13, 34, 56]. There is a complex interplay between the viral dynamics of HIV-1 within the brain and within the plasma and mathematical modeling may be able to uncover new insight.

Materials and Methods

Data

The data used in this study was obtained by digitizing results from published literature [44, 45]. In the published experiment [44, 45], three male rhesus macaques (*Macacamulatta*) were infected intravenously with a mixture of simian-human immunodeficiency virus ($SHIV_{KU-1B}$ and $SHIV_{89-6P}$) and simian immunodeficiency virus (SIV_{17E-Fr}). These animals were monitored for a period of 12 weeks, and levels of circulating $CD4^+$ T cells and viral loads in both the CSF and plasma were measured as described in Kumar *et al.* [45].

Mathematical Model

In the circulation, one of the primary target cells of HIV-1 are uninfected CD4+ T cells (T). These cells become infected (T^*) by free virions (V) within the circulation at a rate β. Infected CD4+ T cells die at a rate δ per day and produce

virions at a rate of p per day per infected cell [74]. Uninfected T cells die at a rate d and are generated at a rate λ.

The major cells that HIV-1 infects in the brain are macrophages [18, 32, 42]. To model this we include an uninfected population of macrophages (M) in the circulation that becomes infected (M^*) upon interaction with free virus at a rate β_M. These infected macrophages produce free virions at a rate p_M per day per infected cell and die at a rate of δ_M per day. Uninfected macrophages die at a rate of d_M and are generated at a rate λ_M. Note that the population of macrophages has been considered to contribute to viral persistence because of its longer lifespan [18, 24, 27, 31, 41, 43, 28, 57].

In order for a virion to enter the CSF in the brain it must pass through the BBB. It is not fully understood what factors modulate transit of HIV-1 RNA through the BBB into the CNS [31]. However studies show that the virus permeates the integrity of the BBB only via an infected macrophage [9, 42]. We represent the rate of the macrophage transit through the BBB by φ. Macrophages are not known to generate independently within the brain [53]. The uninfected brain-macrophages become infected (M_B^*) by the virus in the brain [12, 43, 50, 53, 59] at a constant rate β_M. These infected brain-macrophages produce free virions within the brain at a constant rate p_M per infected cell per day. The free virions in the brain have been shown to possess different characteristics than those within the blood [46, 50, 53] and we classify HIV-1 virions within the brain as V_B. We assume that the free virions V and V_B are both cleared at the same per capita rate c. While limited evidence suggests the possible presence of HIV-1-infected T cells within the CSF [68], because

the primary targets of HIV-1 within the brain are macrophages [41, 42], we consider only macrophages within the brain. Macrophages come out of the brain through the BBB into the bloodstream at a constant rate ψ.

Considerable debate exists regarding whether or not viral replication occurs within the brain [12, 24, 27, 31, 59]. To perform deeper analysis from the modeling point of view, we develop three different variations of the model by introducing a parameter α, which represents the fraction of infectivity (β_M) reduced in the brain compared to outside of the brain. Model 1 ($\alpha = 0$) assumes that viral replication occurs within the brain at the same rate (β_M) as in the bloodstream. Similarly, model 2 ($\alpha = 1$) assumes that no viral replication occurs in the brain, and model 3 ($0 < \alpha < 1$) assumes that the viral replication occurs at a lesser rate than outside of the brain. Since the CSF viral load is significantly less than the plasma viral load, we do not consider the case in which $\alpha > 1$. The schematic diagram of the model is shown in Fig 5. The model equations we use are as follows.

$$
\begin{aligned}
\frac{\mathrm{d}T}{\mathrm{d}t} &= \lambda - \beta V T - dT, \\
\frac{\mathrm{d}T^*}{\mathrm{d}t} &= \beta V T - \delta T^*, \\
\frac{\mathrm{d}M}{\mathrm{d}t} &= \lambda_M + \psi M_B - \beta_M V M - \varphi M - d_M M, \\
\frac{\mathrm{d}M^*}{\mathrm{d}t} &= \beta_M V M + \psi M_B^* - \varphi M^* - \delta_M M^*, \\
\frac{\mathrm{d}M_B}{\mathrm{d}t} &= \varphi M - \psi M_B - (1-\alpha)\beta_M V_B M_B - d_M M_B, \\
\frac{\mathrm{d}M_B^*}{\mathrm{d}t} &= (1-\alpha)\beta_M V_B M_B - \psi M_B^* + \varphi M^* - \delta_M M_B^*, \\
\frac{\mathrm{d}V}{\mathrm{d}t} &= pT^* + p_M M^* - cV, \\
\frac{\mathrm{d}V_B}{\mathrm{d}t} &= p_M M_B^* - cV_B.
\end{aligned}
\tag{3.1}
$$

Three variants of the model are Model 1: $\alpha = 0$; Model 2: $\alpha = 1$; Model 3: $0 < \alpha < 1$.

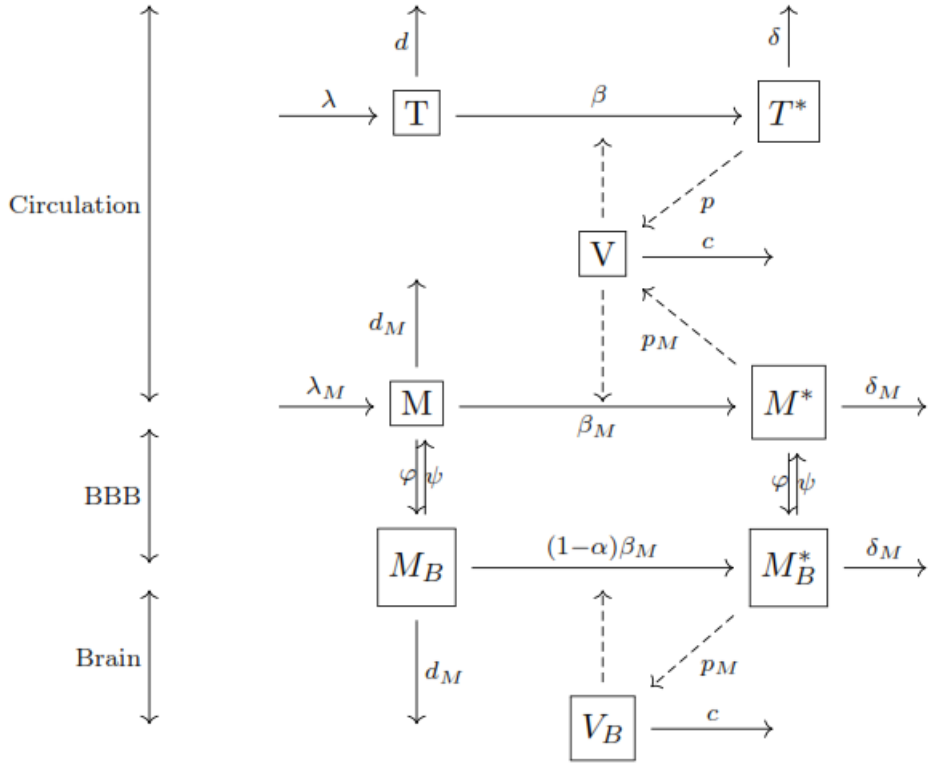

Figure 5: **The schematic diagram of the model representing HIV-1 infection in the brain.** The boxes represent a cell population, the solid arrows represent transport from one population to another, and the dashed arrows represent the cause for the corresponding events.

Parameter Estimation and Data Fitting

We take $T_0 = 38700$ as in Vaidya *et al.* [73]. From Haney *et al.* [30] we estimate $M_0 = 1463000$ and $M_{B0} = 20000$. As estimated by Stafford *et al.* [67], the average life span of uninfected target T cells is 100 days, which implies $d = 0.01$ per day. Macrophages begin their life cycle as monocytes, and there are varying results

regarding the age of the monocyte/macrophage lifespan ranging from three months to three years [53]. We take the average lifespan to be approximately 18 months, i.e. $d_M \sim 0.002$ per day. As every macaque was uninfected at the beginning of the study, we take all infected cells to be zero, i.e., $T_0^* = M_0^* = M_{B0}^* = 0$ [45]. Chen *et al.* [16] estimated the SIV burst size *in vivo* in rhesus macaques as approximately 5×10^4 virions per infected cell, and the infected cell lives approximately one day, thus we take $p = 50,000$. Assuming a steady state before infection, we use $\lambda = dT_0$ and $\lambda_M = d_M(M_0 + M_{B0})$ to estimate λ and λ_M. Schwartz *et al.* [73] estimated the rate of lentiviral production by an infected macrophage to be approximately 1000 virions per infected cell per day. Therefore, we set $p_M = 1000$ for our base case computation. The virion clearance rate during chronic infection in humans varies from 9.1 to 36.0 [54]. Thus we take the average $c = 23$ per day as the minimal estimate. However, we acknowledge that this rate may be higher in macaques.

We estimate the remaining parameters $\beta, \beta_M, \delta, \delta_M, \varphi, \psi$ by fitting the model to the viral load data in the CSF and the plasma. We solve the system of ordinary differential equations (ODEs) numerically using the "ode15s" solver in MATLAB. The predicted $\log_{10}$ values were fitted to corresponding log-transformed viral load data using the nonlinear least square regression, in which the sum of the square residuals, that is, the difference between the model predictions and the corresponding experimental data, is minimized. We used the following formula to calculate the sum of the squared residuals:

$$J = \frac{1}{P}\sum_{i=1}^{P}\left(\log_{10} V(t_i) - \log_{10} \bar{V}(t_i)\right)^2 + \frac{1}{N}\sum_{i=1}^{N}\left(\log_{10} V_B(t_i) - \log_{10} \bar{V}_B(t_i)\right)^2, \quad (3.2)$$

where P and N represent the total number of data points in the plasma and in the brain, respectively. V and $\bar{V}$, represent the virus concentrations in the plasma predicted by the model and those measured in the experimental data, respectively, while V_B and $\bar{V}_B$ represent the virus concentrations in CSF predicted by the model and those measured in the experimental data, respectively. For each best fit parameter estimate, we provide 95% confidence intervals (CI), which were computed from 500 replicates by bootstrapping the residuals [11, 23].

Results

Model Selection

We fit the model to the data containing plasma viral load and the CSF viral load for each of the three monkeys. To compare models we used the Akaike information criterion (AIC) described by the following formula [6].

$$AIC = n \log\left(\frac{J}{n}\right) + \frac{2n(N_p + 1)}{n - N_p - 2}, \tag{3.3}$$

where $n = P + N$ represents the total number of data points considered, J is the sum of the squared residuals (SSR), and N_p represents the number of parameters estimated through data-fitting. The SSR and the AIC values for each of the model 1, model 2, and model 3 are given in Table 1. Note that the lower the AIC value, the better the model fit.

There is no significant difference in the AIC or SSR value between Model 1 and Model 2, but Model 3 has the highest AIC values (Table 1). This indicates that Model 3 does not explain the data well compared to the other models. While we acknowledge that the AIC values do not significantly differ between Model 1 and

Table 1: SSR and AIC values for each of the model 1 ($\alpha = 0$), model 2 ($\alpha = 1$), and the model 3 ($0 < \alpha < 1$) fitted to each of the three monkeys.

	Model 1 ($\alpha = 0$)		**Model 2** ($\alpha = 1$)		**Model 3** ($0 < \alpha < 1$)	
	SSR	**AIC**	**SSR**	**AIC**	**SSR**	**AIC**
Monkey 1	4.6235	17.1562	4.4903	16.7469	3.8943	26.8866
Monkey 2	2.4144	55.788	2.4163	55.7966	2.4159	145.7951
Monkey 3	4.9797	18.1952	4.9758	18.1841	4.9781	30.3239

Model 2, Model 1 is supported by the previous study by Schnell [59], in which the rate of infectivity for macrophages in the brain is the same as that outside the brain. Therefore, we select the model 1 to present the subsequent results in the sections to follow.

The prediction of the selected model, i.e. Model 1, along with the data for each of the three monkeys are shown in Fig. 6. Our model agrees well with the data (Fig. 2). The estimated parameters are given in Table 2.

Rates of Infection and Cell Death

We estimated that the rate, β, at which the virus infects CD4+ T cells, ranges between 2.58×10^{-8} and 4.40×10^{-8} viral RNA copies per ml per day. These estimates are consistent with the previous estimates [74]. The infection rate estimated for macrophages, β_M, ranges between 4.01×10^{-11} and 1.00×10^{-9} viral RNA copies per ml per day, implying that macrophages are less susceptible to viral infection than CD4+ T cells. Similarly, we found that the death rate of infected macrophage

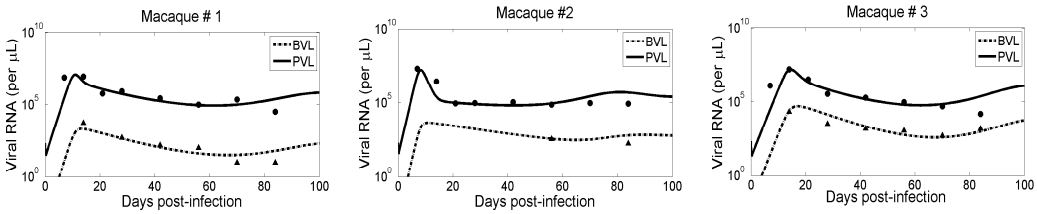

Figure 6: **Model fit to the data**. Plasma viral load (solid line) and CSF viral load (dashed line) predicted by the selected model, i.e. Model 1, along with the experimental data (filled circle: plasma viral load; filled triangle: CSF viral load) from three monkeys [44, 45].

(median $\delta_M \sim 0.21$ per day) is significantly lower than the death rate of infected CD4+ T cells (median $\delta \sim 1.61$ per day). Thus our model suggests that infected macrophages persist with the virus far longer than infected T cells, which is consistent with findings from previous experiments [43, 51, 53].

Reproduction Number

The basic reproduction number ($\mathfrak{R}_0$) is defined as the average number of secondary infected cells produced by a single infected cell when there is no target cell limitation [76]. In viral dynamics, the basic reproduction number is an important threshold that can determine whether infection occurs. Specifically, if $\mathfrak{R}_0 < 1$ the infection dies out, and if $\mathfrak{R}_0 > 1$ the infection occurs [76]. For our model we use the next-generation method [22, 76] to compute $\mathfrak{R}_0$.

Our model possesses a unique infection-free equilibrium (IFE), given by

$$(T_*, 0, M_*, 0, M_{B*}, 0, 0, 0),$$

where

$$T_* = \frac{\lambda}{d},$$

$$M_* = \frac{\lambda_M(\psi + d_M)}{(\varphi + d_M)(\psi + d_M) - \psi\varphi}, \qquad \text{and}$$

$$M_{B*} = \frac{\lambda_M \varphi}{(\varphi + d_M)(\psi + d_M) - \psi\varphi}.$$

Following the next generation matrix method, we linearize the five model equations corresponding to infection classes, *i.e.*, T^*, M^*, M_B^*, V, and V_B, about the IFE and introduce the following matrices:

$$F = \begin{bmatrix} 0 & 0 & 0 & \frac{\beta\lambda}{d} & 0 \\ 0 & 0 & 0 & \frac{\beta_M \lambda_M(\psi+d_M)}{(\varphi+d_M)(\psi+d_M)-\psi\varphi} & 0 \\ 0 & 0 & 0 & 0 & \frac{\beta_M \lambda_M \varphi}{(\varphi+d_M)(\psi+d_M)-\psi\varphi} \\ p & p_M & 0 & 0 & 0 \\ 0 & 0 & p_M & 0 & 0 \end{bmatrix},$$

and

$$V = \begin{bmatrix} \delta & 0 & 0 & 0 & 0 \\ 0 & \varphi + \delta_M & -\psi & 0 & 0 \\ 0 & -\varphi & \psi + \delta_M & 0 & 0 \\ 0 & 0 & 0 & c & 0 \\ 0 & 0 & 0 & 0 & c \end{bmatrix},$$

where F represents a matrix of new infections and/or viral production in the linearized system and V represents a matrix of the transfer of cell or virus into and out of the compartment. The basic reproduction number is then given by the spectral

radius of FV^{-1}. That is,

$$\mathfrak{R}_0 = \frac{1}{2\varphi\psi AD} \cdot \left[\sqrt{2}\sqrt{\varphi\psi AD\left(AB + CE + \sqrt{(AB)^2 + HC^2 + C(B+C)G + BC\Psi}\right)}\right],$$

where

$$A = \frac{\varphi^2 + \delta_M\varphi + d_M\varphi + 2\varphi\psi + \psi^2 + \delta_M\psi + d_M\psi + d_M\delta_M}{\varphi\psi}, \qquad B = p\beta\lambda\delta_M d_M\varphi\psi,$$

$$C = p_M\beta_M\lambda_M\delta d\varphi\psi, \qquad D = d_M c\delta d\delta_M, \qquad E = \varphi^2 + 2\delta_M\varphi + \varphi\psi + d_M\psi + d_M\delta_M,$$

$$G = \frac{\varphi^4 + (\varphi\psi)^2 + 2d_M\psi(\varphi^2 + \delta_M\varphi + d_M\delta_M)}{(\varphi\psi)^2}, \qquad H = \frac{1 + \psi^2 - 2d_M\delta_M\varphi^2 + 2d_M\varphi\psi^2}{(\varphi\psi)^2},$$

and

$$\Psi = \frac{1}{(\varphi\psi)^2}\left(-3\varphi^4 - 2\varphi^2\psi + (d_M + \delta_M)(-2\varphi^3 + 2d_M\psi(\psi + \delta_M))\right.$$

$$\left. +2(\varphi + d_M)(\psi^3 + d_M\delta_M) + (\varphi\psi)^2 + 2d_M\delta_M(\psi^2 + d_M\delta_M)\right).$$

We now use the parameters estimated above to obtain the basic reproduction number for each monkey. We found that $\mathfrak{R}_0$ ranges from 1.33 to 1.55. Note that $\mathfrak{R}_0 > 1$ in each case as expected because the experimental data show that the infection persists in each monkey. We further perform the sensitivity analysis to identify how sensitive the value of $\mathfrak{R}_0$ is to each parameter. To quantify the sensitivity we considered the sensitivity index S_x [58], given by

$$S_x = \left(\frac{X}{\mathfrak{R}_0}\right)\left(\frac{\partial\mathfrak{R}_0}{\partial X}\right),$$

where X is a parameter whose sensitivity is sought. Based on the S_x values (Fig. 7), we identified that the parameters d, β, p, c, δ, and λ have the greatest influence on $\mathfrak{R}_0$, whereas $\varphi, \psi, d_M, \beta_M, p_M, \delta_M, \lambda_M$ have much less effect. We observe that the

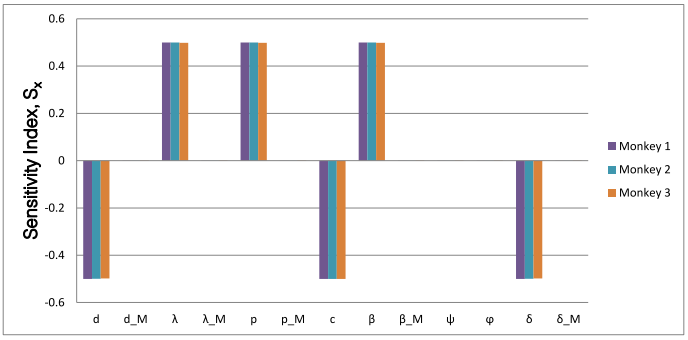

Figure 7: **Sensitivity of Parameter Estimations to $\mathfrak{R}_0$**

parameters greatly influencing $\mathfrak{R}_0$ are mostly T cell related. Thus the T cell and related parameters are primary contributors to the initial establishment of the viral infection.

Transport Through the BBB

Regarding infection in the brain, the transport of virus through BBB plays a critical role. These mechanisms can be studied through the parameters φ and ψ of our model. Our estimates show that the per capita rate of macrophage entry into the brain, $\varphi \sim 0.29$ per day, is significantly less than the per capita rate of macrophage exit from the brain, $\psi \sim 9.41$ per day (Table 2). This implies that the transport of virus out of the brain via infected macrophages can be greater than the transport of virus into the brain. As a result, the amount of virus, which replicates inside the brain and then exits into the bloodstream through the BBB, can be significantly high. Thus the brain may act as an HIV-1 reservoir supplying HIV-1 into the bloodstream causing the persistent infection despite control of virus in the bloodstream through successful treatment.

Because of potential selection imposed by the BBB, especially for the entry of virus into the brain, we ask a question whether inflow of virus into the brain is constant and thus the brain compartment can be studied in isolation as done in some previous study [56]. To analyze viral entry into the brain we calculated the rate of number of infected macrophages (φM^*) entered into the brain over time for 100 days post-infection (Fig. 8). The model prediction suggests that infected macrophages enter the brain through the BBB at time-varying rate, depending upon the infection outside the brain. This indicates that the brain and the plasma must be considered as one coupled system rather than two separate ones to accurately predict the viral dynamics in the brain, at least during the acute phase of infection.

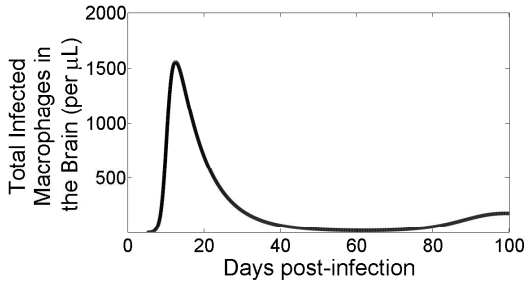

Figure 8: **Incoming infected macrophages entering the brain (φM^*).** Model simulations of the total count of infected macrophages (φM^*) entering the brain for 100 days post-infection.

Cell and Virus Dynamics

We first used our model to study the acute phase dynamics of macrophages (Fig. 9). The infected macrophages in the plasma and the brain both reach a peak at approximately 18 days post-infection, and then decline steadily over the next three weeks, eventually reaching a set point level. The dynamics of infected macrophages in the brain is similar to that of the infected macrophages in the plasma, however the amount of infected macrophages in the brain is significantly lower (peak at ≈ 170 per μL) than the infected macrophages in the plasma (peak at $\approx 40,000$ per μL). This small amount of infected macrophages hiding inside the brain may explain the low level of viral persistence during the treatment of infected patients as many drugs cannot enter the brain through the BBB [46]. The uninfected macrophages, both in the brain and in the plasma, decline rapidly (by $\approx 6\%$) of their initial amounts.

We also studied a long-term dynamics by performing model simulations for 1000 days (approximately 3 years). After approximately 200 days the CD4+ T cell count, the infected macrophages in the brain and the plasma, and the viral RNA copies in the brain and the plasma all reach a steady state (Fig 10). The steady state level of the infected macrophages in the brain is roughly one fourth of that outside the brain (200 per μL outside vs 50 per μL inside the brain). Similarly, the steady-state level of viral RNA in the brain is nearly threefold less than that in the plasma ($\approx 10^3$ vRNA copies in the brain vs. $\approx 10^6$ vRNA copies in the plasma), consistent with the experimental results [45]. The CD4+ count drops rapidly and levels off at 400 shortly after day 200.

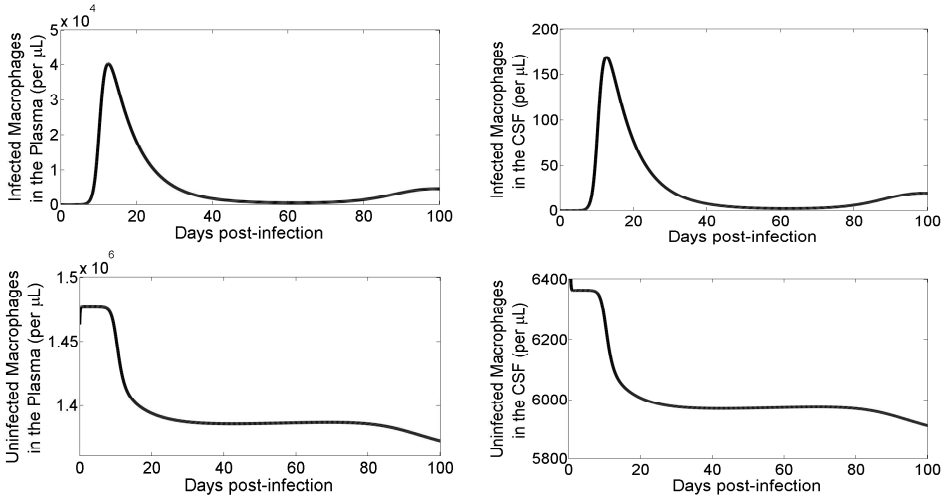

Figure 9: **Simulations of macrophages in the plasma and the CSF.** Model simulations over 100 days post-infection of infected macrophages (top row) and uninfected macrophages (bottom row) in the plasma (left column) and in the brain (right column).

Sensitivity Analysis

Sensitivity of data-fitting estimates on the fixed parameters. Our data-fitting estimates were based on the fixed values of parameters M_0, M_{B0}, d_M, and p_M. While we estimated values of these parameters from the literature, there is uncertainty with these values. Therefore, we performed the sensitivity of the data-fitting parameter estimates to the choice of the initial conditions M_0 and M_{B0} (Fig. 11) and the choice of d_M and p_M (Fig. 12).

First, we performed 200 different data fittings using M_0 and M_{B0} values chosen randomly from the uniform distribution between 10% less and 10% more values than the base value. We observed that the median change in the estimated parame-

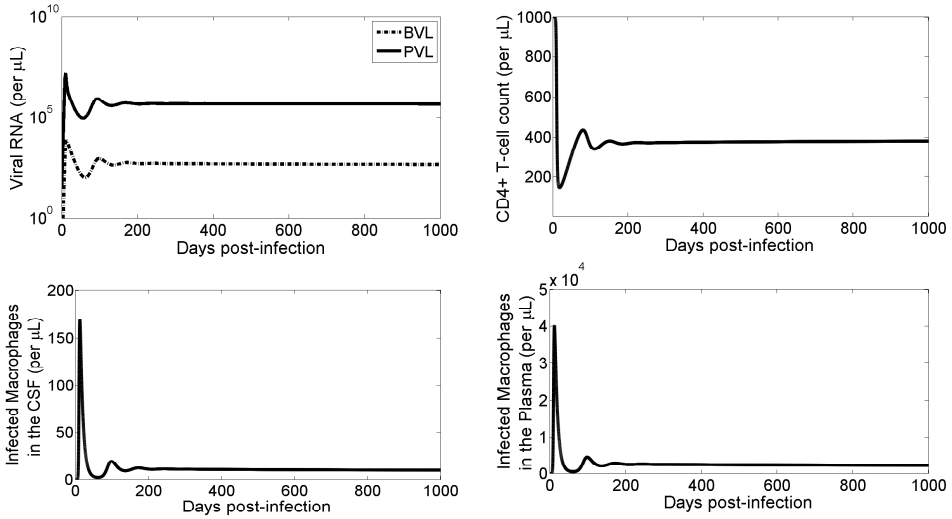

Figure 10: **Long-term model simulations.** Viral load (top left) for the plasma (solid line) and the brain (dashed line) along with the CD4+ T cell count (top right) and the total infected macrophages (bottom row) in the brain (bottom left) and in the plasma (bottom right).

ters remained below 10% for each parameter and for each monkey except for β_M in Monkey 2 (22% change) (Fig. 11). This high sensitivity of β_M for Monkey 2 is likely due to the lack of enough data points in the brain for this monkey. The overall mean change of each estimated parameter also remained less than 10% from the base case estimate, suggesting our estimates were robust within these ranges of M_0 and M_{B0}.

Then, we also performed 200 data fittings using d_M and p_M values sampled randomly from the values between 10% less and 10% more than the base values. In this case, we observed that both the median and the mean change in the estimated parameters never exceeded more than 8% for each parameter for each monkey. This

suggests that our parameter estimates for d_M and p_M were also robust within these ranges for d_M and p_M.

Sensitivity of model dynamics on the general parameter space. Given the limited number of data sets and extreme complications for the study of brain virus, the results based on the model dynamics from our limited estimates require further analysis on a wider parameter space. To examine the robustness of our model dynamics we performed 200 simulations using a Latin hypercube sampling (LHS) of nine parameters (δ_M, ψ, φ, β_M, β, M_{B0}, M_0, p_M, and d_M). The box-plots and partial rank correlation coefficients of this sensitivity analysis is shown in Fig. 13 and 14, respectively. The dynamics from the data fitting estimates (solid lines) are clearly captured within the boxes of the LHS results. Predicted dynamics are more sensitive to the parameters during early part of the infection. Variation of the viral dynamics in the brain is much wider than that in the plasma (Fig. 13).

We calculated PRCC values at weeks one, two, three, and 26, corresponding to the timings for pre-peak, peak, post-peak, and set point viral load, respectively (Fig. 14). The computed partial rank correlation coefficients indicate that, parameters, in general, have stronger correlation to the viral load in the CSF compared to that in the plasma. Both plasma and CSF viral load are most correlated with parameters related to infection rates, β_M and β, and macrophage life-span, δ_M. In addition, the CSF viral load is highly correlated with the BBB related parameter, φ. These parameters, except δ_M, mainly have larger effect on early viral load than in the late viral load. Both plasma and CSF viral loads are positively impacted by β_M and β, and negatively impacted by δ_M, while φ has positive impact on CSF viral load and

Table 2: **Parameter estimates through data fitting.** Estimated parameters from fitting the selected model, i.e. Model 1, to each of the three monkey's data. Paired values in parentheses represent 95% confidence intervals.

	δ day^{-1}	δ_M day^{-1}	φ day^{-1}	ψ day^{-1}	β ml/day	β_M ml/day
Monkey 1	1.7319 (0.5555,1.8049)	0.2067 (0.1405,0.4141)	0.0117 (0.00220,0.22342)	9.4052 (8.2458,10.8779)	3.7332E-8 (1.9456E-8,7.4280E-8)	1.0018E-9 (9.9297E-10,1.0000E-9)
Monkey 2	1.6129 (0.8940,1.8214)	0.0673 (0.0234,0.1256)	0.78565 (0.33675,2.3305)	15.0023 (14.4669,15.2483)	4.4009E-8 (3.5322E-8,7.3811E-8)	4.0068E-11 (1.0000E-11,4.0119-11)
Monkey 3	1.0766 (0.5941,1.1664)	0.2127 (0.1550,0.2797)	0.29149 (0.08801,0.91395)	8.8010 (8.6176,9.0556)	2.5809E-8 (1.8701E-8,2.6271E-8)	6.9003E-10 (3.5739E-10,9.3840E-10)

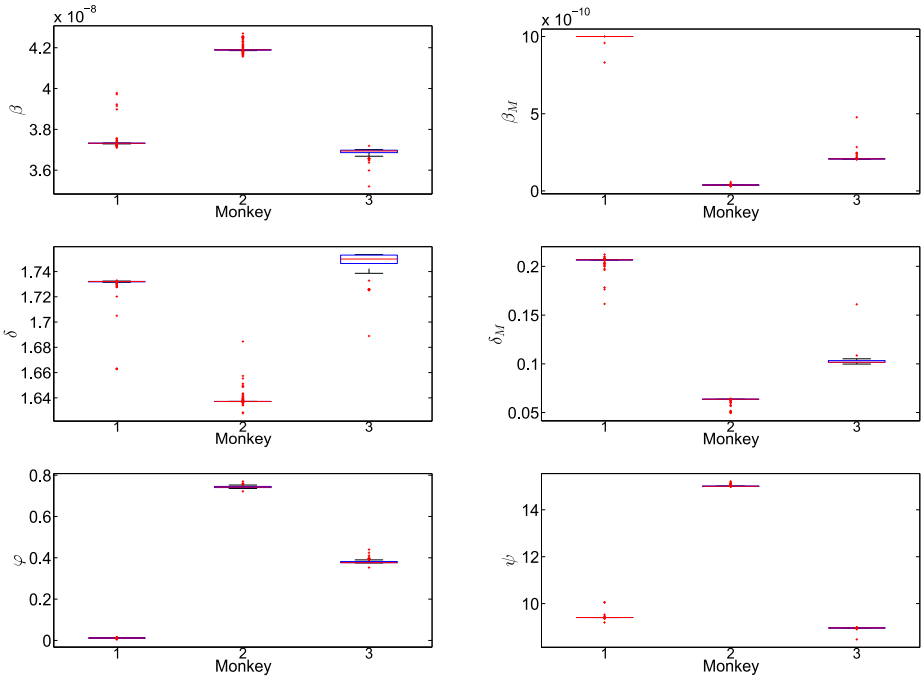

Figure 11: **Box-plots of the parameter estimates from 200 data-fittings with values of M_0 and M_{B0} selected randomly from $\pm 10\%$ of the base values.** Each subfigure represents the result for one of the parameters estimated.

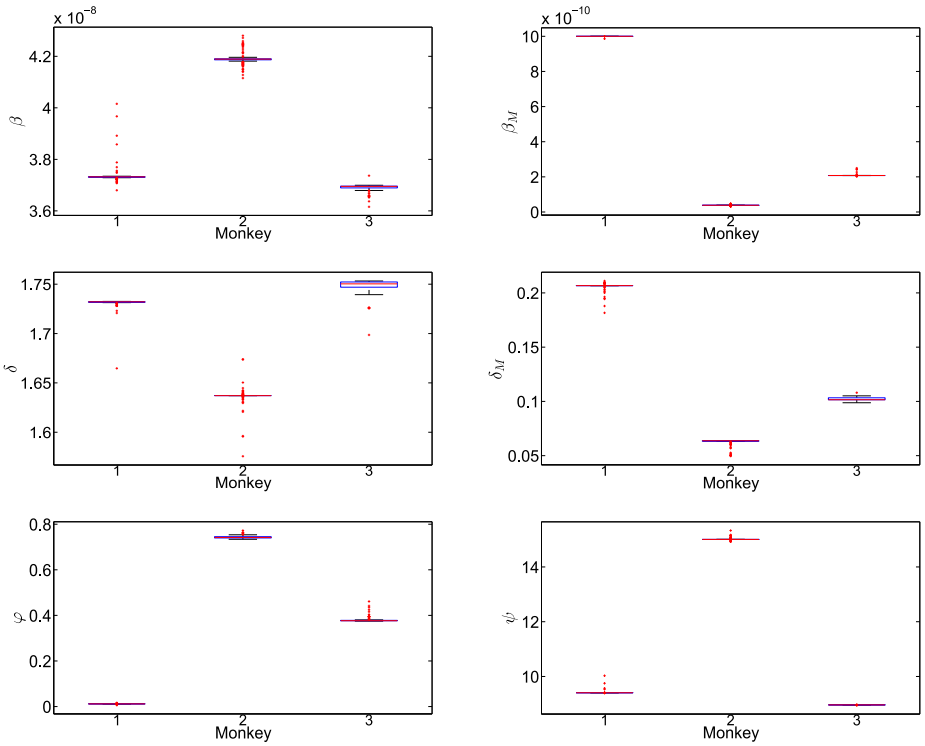

Figure 12: **Box-plots of the parameter estimates from 200 data-fittings with values of d_M and p_M selected randomly from $\pm 10\%$ of the base values.** Each subfigure represents the result for one of the parameters estimated.

negative impact (but with smaller magnitude) on the plasma viral load.

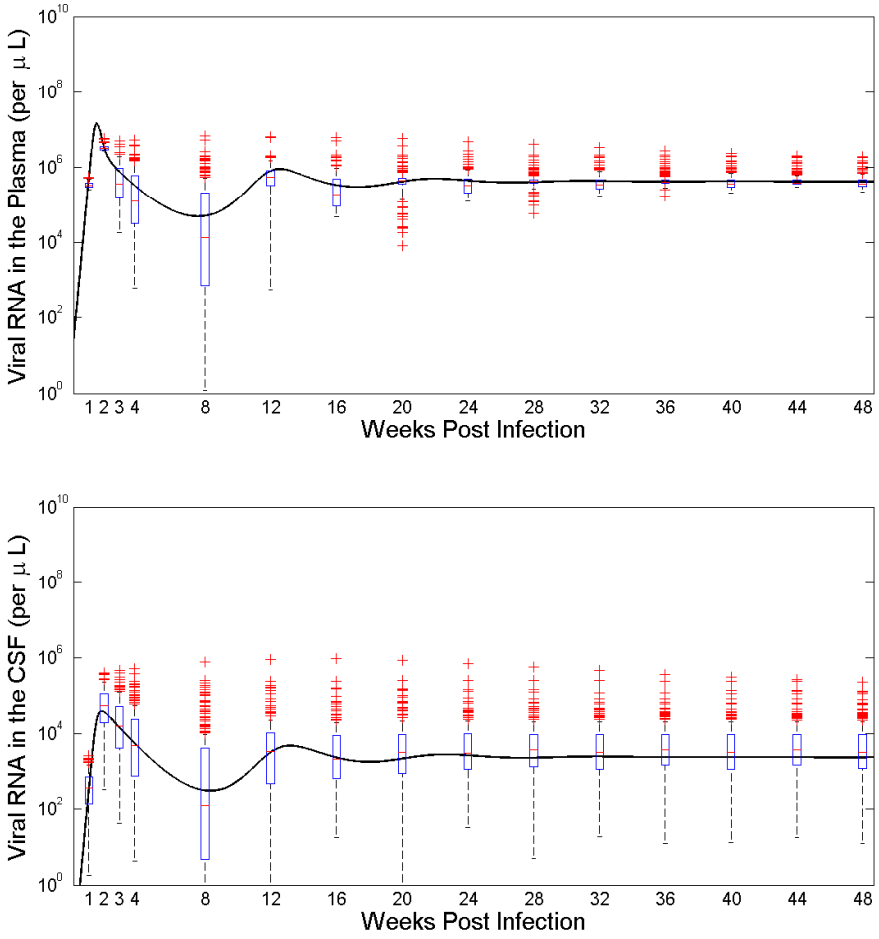

Figure 13: **Box-plots of the results of 200 simulations of the Model from Latin hypercube sampling.** The sensitivity of the dynamics of plasma viral load (top) and the CSF viral load (bottom) based on 200 Latin Hypercube sampling. The black sold line represents the viral dynamics predicted by the model with median parameters estimated from three monkey data.

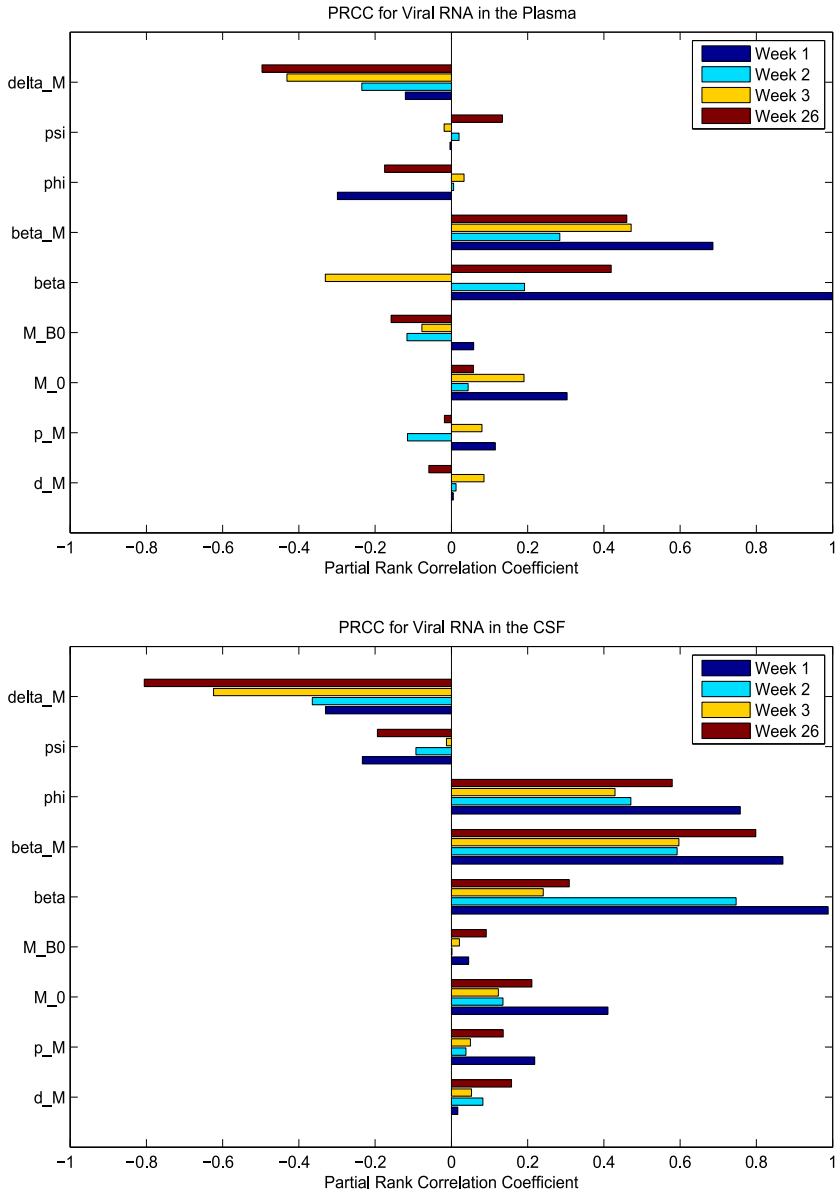

Figure 14: **Partial rank correlation coefficients from the Latin hypercube sampling method.** PRCC values of the plasma (top) and the CSF (bottom) viral loads at weeks 1 (pre-peak), 2 (peak), 3 (post-peak), and 26 (set-point) post infection.

CHAPTER 4

EFFECTS OF THE BLOOD-BRAIN BARRIER ON THE TREATMENT OF HIV-INFECTION IN THE BRAIN

In this chapter we develop a mathematical model to analyze the effect of the BBB on the overall treatment of HIV in the brain. We consider ART by varying key drug parameters such as the CPE score, the slope of the dose-response curve, and the initial treatment date. We also analyze the model to establish the local and global properties of the infection dynamics. We show how varying the slope of the dose-response curve, the CPE score, and the time of treatment initiation affects the viral loads in the plasma and in the brain, and the time that viral loads become undetectable.

Introduction

In Chapter 3, we developed a model that adequately described the viral dynamics of HIV-1 in the brain. We obtained interesting results that suggested new parameters to measure the transport of macrophages through the BBB. These results provided the need to examine the effect of the BBB on the treatment of HIV-1. Current ART drugs fail to fully penetrate through the BBB, resulting in reduced efficacy in the brain. Thus it is important to study what effects this reduced drug efficacy in the brain may impose on the overall treatment of HIV-1.

Model

Model Development

We develop a model with treatment by incorporating treatment terms into the model previously developed in Chapter 3. We describe the viral dynamics using the following differential equations, and a schematic diagram of the model is presented in Figure 15. All parameter values are given in Table 3.

$$
\begin{aligned}
\frac{\mathrm{d}T}{\mathrm{d}t} &= \lambda - \prod_{i=1}^{n}(1-\varepsilon_i)\beta V T - dT, \\
\frac{\mathrm{d}T^*}{\mathrm{d}t} &= \prod_{i=1}^{n}(1-\varepsilon_i)\beta V T - \delta T^*, \\
\frac{\mathrm{d}M}{\mathrm{d}t} &= \lambda_M - \prod_{i=1}^{n}(1-\varepsilon_i)\beta_M V M - \varphi M + \psi M_B - d_M M, \\
\frac{\mathrm{d}M^*}{\mathrm{d}t} &= \prod_{i=1}^{n}(1-\varepsilon_i)\beta_M V M + \psi M_B^* - \varphi M^* - \delta_M M^*, \\
\frac{\mathrm{d}M_B}{\mathrm{d}t} &= \varphi M - \psi M_B - \prod_{i=1}^{n}(1-\varepsilon_{\pi i})\beta_M V_B M_B - d_M M_B, \\
\frac{\mathrm{d}M_B^*}{\mathrm{d}t} &= \prod_{i=1}^{n}(1-\varepsilon_{\pi i})\beta_M V_B M_B - \psi M_B^* + \varphi M^* - \delta_M M_B^*, \\
\frac{\mathrm{d}V}{\mathrm{d}t} &= \prod_{i=1}^{}(1-\varepsilon_{PIi})\, pT^* + \prod_{i=1}^{}(1-\varepsilon_{PIi})\, p_M M^* - cV, \\
\frac{\mathrm{d}V_B}{\mathrm{d}t} &= \prod_{i=1}^{}(1-\varepsilon_{\pi PIi})\, p_M M_B^* - cV_B.
\end{aligned}
\tag{4.1}
$$

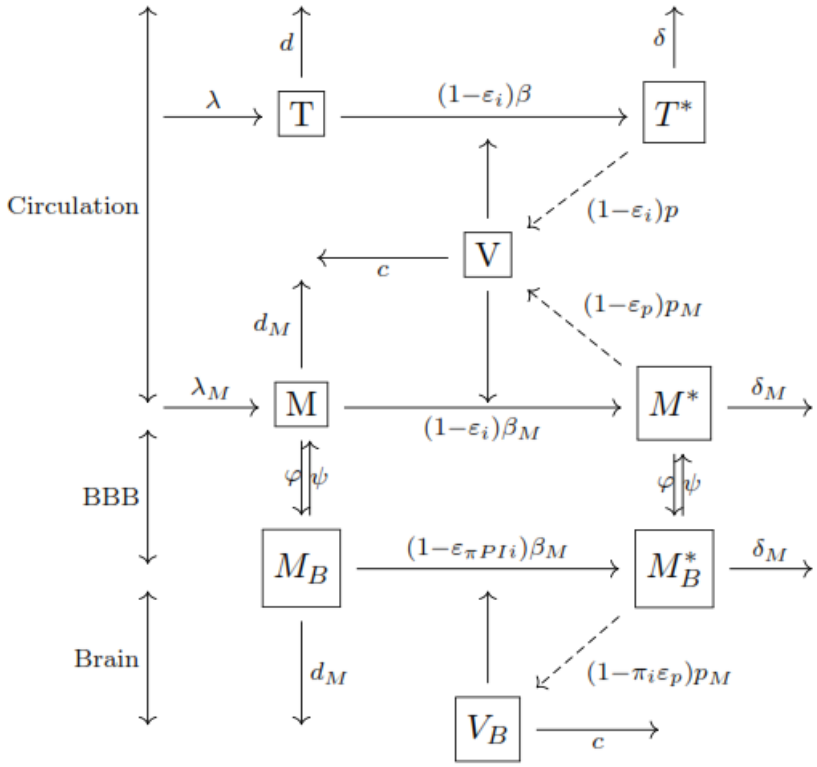

Figure 15: Schematics for model with treatment

Currently there are five available classes of ART drugs: Fusion Inhibitors (FIs), Nucleoside reverse transcriptase inhibitors (NRTIs), Non-nucleoside reverse transcriptase inhibitors (NNRTIs), Integrase inhibitors (IIs), and Protease inhibitors (PIs) [4]. The efficacy of each drug, ε, can be calculated by the formula [75]:

$$\varepsilon = 1 - \left(\frac{1}{1 + \left(\frac{D}{ED_{50}} \right)^m} \right),$$

where m is Hill's coefficient, D is the amount of drug concentration present, and ED_{50} represents the concentration of drugs required to obtain 50% of the maximal

effect. Note that Hill's coefficient is also considered to be the slope of the dose-response curve of a given drug. ART drugs reduce the respective viral production rates p, and p_M to $(1-\varepsilon_{PIi})p$ and $(1-\varepsilon_{PIi})p_M$, in the case of PIs, or reduce the infection rates β, and β_M to $(1-\varepsilon_i)\beta$ and $(1-\varepsilon_i)\beta_M$, respectively, for other drug classes. When multiple drugs are used in treatment, the net reduction is given by the product of drug effectiveness values, that is, for FIs, IIs, and RTIs, the infection rates are reduced to $\prod_{i=1}^{n}(1-\varepsilon_i)\beta$ and $\prod_{i=1}^{n}(1-\varepsilon_i)\beta_M$, and for PIs the viral production rates are reduced to $\prod_{i=1}^{n}(1-\varepsilon_{PIi})p$ and $\prod_{i=1}^{n}(1-\varepsilon_{PIi})p_M$.

The BBB reduces the net effectiveness of ART drugs by limiting the amount of concentration into the CSF. A study by Letendre *et al.* [46] examined the viral loads in the CSF in the presence of ART drugs and created a standard measure (CNS penetration effectiveness score, or CPE-score) for the effectiveness of an ART drug at entering the brain. Based on this study, we construct the parameter, π, to represent this dampening effect as follows:

$$\pi = \frac{\text{CPE Score}}{5},$$

where the CPE score (or CNS penetration effectiveness score) ranges from zero to five. In particular, for drugs crossing the BBB we have

$$\varepsilon_\pi = 1 - \left(\frac{1}{1 + \left(\frac{\pi D}{ED_{50}} \right)^m} \right).$$

Here a lower CPE score implies a lower concentration of the ART drug in the CSF. For our purposes we consider a score of five to means that a drug maintains an equal effectiveness in the brain as it does in the plasma. Similarly, a minimum score of zero

implies that the drug cannot penetrate through the BBB.

Model Analysis

For ease of notation we now define the following variables:

$$\Phi_b = \prod_{i=1}^{n} (1 - \varepsilon_i)\,, \qquad \Phi_p = \prod_{i=1}^{n} (1 - \varepsilon_{PIi}), \text{ and}$$

$$\Phi_{\pi b} = \prod_{i=1}^{n} (1 - \varepsilon_{\pi i}), \qquad \Phi_{\pi p} = \prod_{i=1}^{n} (1 - \varepsilon_{\pi PIi}).$$

Model Feasibility

In view of [65, Theorem 5.2.1], it follows that for any

$$(T_0, T_0^*, M_0, M_0^*, M_{B0}, M_{B0}^*, V_0, V_{B0}) \in \mathbb{R}_+^8,$$

system (4.1) has a unique local nonnegative solution

$$(T(t), T^*(t), M(t), M^*(t), M_B(t), M_B^*(t), V(t), V_B(t)) \in \mathbb{R}_+^8$$

through the initial value:

$$(T(0), T^*(0), M(0), M^*(0), M_B(0), M_B^*(0), V(0), V_B(0))$$

$$= (T_0, T_0^*, M_0, M_0^*, M_{B0}, M_{B0}^*, V_0, V_{B0}).$$

Substituting

$$N(t) = T(t) + T^*(t) + M(t) + M^*(t) + M_B(t) + M_B^*(t) \tag{4.2}$$

into system (4.1), leading to the following inequality

$$\begin{aligned}\frac{dN}{dt} &= \lambda - (dT + \delta T^*) + \lambda_M - d_M(M + M_B) - \delta_M(M^* + M_B^*) \\ &\leq \lambda + \lambda_M - d_{\min}(T + T^* + M + M^* + M_B + M_B^*) \\ &= \lambda + \lambda_M - d_{\min} N,\end{aligned}$$

where $d_{\min} := \min\{d, \delta, d_M, \delta_M\}$, and hence,

$$\lim_{t\to\infty} N(t) \leq \frac{\lambda + \lambda_M}{d_{\min}}. \tag{4.3}$$

This implies that $N(t)$ is ultimately bounded, so are $T(t)$, $T^*(t)$, $M(t)$, $M^*(t)$, $M_B(t)$ and $M_B^*(t)$, due to (4.2) and the positivity of solutions. Then there exist $t_0 > 0$ and $\Lambda > 0$ such that

$$\Phi_p p T^*(t) + \Phi_p p_M M^*(t) \leq \Lambda \text{ and } \Phi_{\pi p} p_M M_B^*(t) \leq \Lambda, \ \forall\ t \geq t_0.$$

From the seventh and eighth equations of (4.1), we see that

$$\frac{dV}{dt} \leq \Lambda - cV, \ \forall\ t \geq t_0,$$

and

$$\frac{dV_B}{dt} \leq \Lambda - cV_B, \ \forall\ t \geq t_0.$$

Thus,

$$\lim_{t\to\infty} V(t) \leq \frac{\Lambda}{c}, \text{ and } \lim_{t\to\infty} V_B(t) \leq \frac{\Lambda}{c},$$

that is, we have shown that $V(t)$ and $V_B(t)$ are ultimately bounded.

From the above discussion and Theorem 3.4.8 in [29], we have the following result:

Theorem 1. *$\mathbb{R}^8_+$ is positively invariant for system* (4.1) *and system* (4.1) *admits a unique and bounded solution with the initial value in $\mathbb{R}^8_+$. Further, system* (4.1) *admits a connected global attractor on $\mathbb{R}^8_+$ which attracts all positive orbits in $\mathbb{R}^8_+$.*

Basic Reproduction Number

We first determine the infection-free equilibrium, E_0, of system (4.1). To this end, we substitute $T^* = M^* = M_B^* = 0$ into system (4.1), and we have $V = V_B = 0$. Furthermore, we arrive at the following systems:

$$\frac{dT}{dt} = \lambda - dT, \tag{4.4}$$

and

$$\begin{cases} \frac{dM}{dt} = \lambda_M - (\varphi + d_M)M + \psi M_B, \\ \frac{dM_B}{dt} = \varphi M - (\psi + d_M)M_B. \end{cases} \tag{4.5}$$

It is easy to see that system (4.4) admits a unique positive equilibrium $\hat{T} := \frac{\lambda}{d}$, which is globally attractive in $\mathbb{R}_+$. We also see that

$$(\hat{M}, \hat{M}_B) = \left(\frac{\lambda_M a}{d_M}, \frac{\lambda_M (1-a)}{d_M} \right) \tag{4.6}$$

is the unique positive equilibrium of system (4.5), where $a = \frac{\psi + d_M}{\varphi + \psi + d_M}$. Since system (4.5) is cooperative (see, e.g., [65]) and it admits a unique positive equilibrium $(\hat{M}, \hat{M}_B)$, we can show the global stability of $(\hat{M}, \hat{M}_B)$ (see, e.g., [36]). The following results are concerned with the dynamics of systems (4.4) and (4.5).

Lemma 1. *The following statements are valid.*

(i) System (4.4) *admits a unique positive equilibrium $\hat{T} := \frac{\lambda}{d}$, which is globally attractive in $\mathbb{R}_+$.;*

(ii) System (4.5) *admits a unique positive equilibrium* $(\hat{M}, \hat{M}_B)$ *which is globally attractive in* $\mathbb{R}^2_+$*, that is, for any* $(M(0), M_B(0)) \in \mathbb{R}^2_+$*, we have*

$$\lim_{t\to\infty}(M(t), M_B(t)) = (\hat{M}, \hat{M}_B).$$

From the above discussions, the infection-free equilibrium of system (4.1) takes the form

$$E_0 = (T, T^*, M, M^*, M_B, M_B^*, V, V_B) = (\hat{T}, 0, \hat{M}, 0, \hat{M}_B, 0, 0, 0).$$

The equations for the infected cells and free virions in the plasma and the brain of the linearized system at the infection-free equilibrium, E_0, take the form

$$\begin{cases} \frac{dT^*}{dt} = \Phi_b\beta\hat{T}V - \delta T^*, \\ \frac{dM^*}{dt} = \Phi_b\beta_M\hat{M}V + \psi M_B^* - (\varphi + \delta_M)M^*, \\ \frac{dM_B^*}{dt} = \Phi_{\pi b}\beta_M\hat{M}_B V_B + \varphi M^* - (\psi + \delta_M)M_B^*, \\ \frac{dV}{dt} = \Phi_p p T^* + \Phi_p p_M M^* - cV, \\ \frac{dV_B}{dt} = \Phi_{\pi p} p_M M_B^* - cV_B. \end{cases} \tag{4.7}$$

The spectral bound or the stability modulus of an $n\times n$ matrix M, denoted by $s(M)$, is defined by

$$s(M) := \max\{\mathrm{Re}(\lambda) : \lambda \text{ is an eigenvalue of } M\}.$$

Motivated by (4.7), we define the following matrix:

$$J = \begin{pmatrix} -\delta & 0 & 0 & \Phi_b\beta\hat{T} & 0 \\ 0 & -(\varphi+\delta_M) & \psi & \Phi_b\beta_M\hat{M} & 0 \\ 0 & \varphi & -(\psi+\delta_M) & 0 & \Phi_{\pi b}\beta_M\hat{M}_B \\ \Phi_p p & \Phi_p p_M & 0 & -c & 0 \\ 0 & 0 & \Phi_{\pi p}p_M & 0 & -c \end{pmatrix}. \tag{4.8}$$

Clearly, J has non-negative off-diagonal elements, and J is irreducible (see a simple test on page 256 of [66]). Then $s(J)$ is a simple eigenvalue of J with a positive eigenvector (see, e.g., [66, Theorem A.5]).

We now use the next generation matrix method [76] to compute the basic reproduction number, $\mathfrak{R}_0$. We introduce the following matrices:

$$F = \begin{pmatrix} 0 & 0 & 0 & \Phi_b\beta\hat{T} & 0 \\ 0 & 0 & 0 & \Phi_b\beta_M\hat{M} & 0 \\ 0 & 0 & 0 & 0 & \Phi_{\pi b}\beta_M\hat{M}_B \\ \Phi_p p & \Phi_p p_M & 0 & 0 & 0 \\ 0 & 0 & \Phi_{\pi p}p_M & 0 & 0 \end{pmatrix}, \tag{4.9}$$

and

$$V = \begin{pmatrix} \delta & 0 & 0 & 0 & 0 \\ 0 & \varphi+\delta_M & -\psi & 0 & 0 \\ 0 & -\varphi & \psi+\delta_M & 0 & 0 \\ 0 & 0 & 0 & c & 0 \\ 0 & 0 & 0 & 0 & c \end{pmatrix}. \tag{4.10}$$

Note that $J = F - V$. The basic reproductive number corresponds to the spectral

radius of FV^{-1},

$$\mathfrak{R}_0 = \rho(FV^{-1}).$$

The following is a general result showing that the local stability of the disease-free equilibrium, E_0, is determined by $\mathfrak{R}_0$ (see, e.g. [76, Theorem 2]):

Lemma 2. *The following statements hold.*

(i) $\mathfrak{R}_0 = 1$ *if and only if* $s(J) = 0$*;*

(ii) $\mathfrak{R}_0 > 1$ *if and only if* $s(J) > 0$*;*

(iii) $\mathfrak{R}_0 < 1$ *if and only if* $s(J) < 0$*.*

Thus, the disease-free equilibrium E_0 *is locally asymptotically stable if* $\mathfrak{R}_0 < 1$*, and unstable if* $\mathfrak{R}_0 > 1$*.*

Clearly the reproduction number is a function of the treatment effectiveness parameters, ε_i and ε_{PIi}. In Figure 16 we show the change in $\mathfrak{R}_0$ based on these parameters as well as the total region in which $\mathfrak{R}_0 \geq 1$ depending on the drug efficacies of ART drugs.

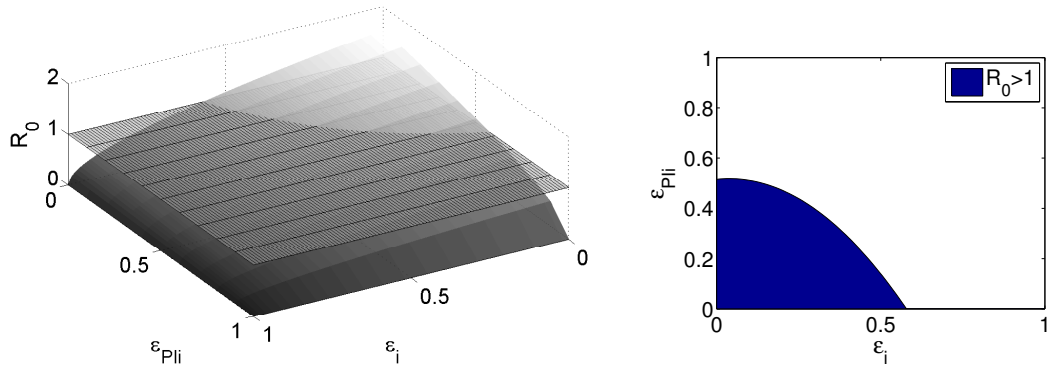

Figure 16: Graph of the reproduction number $\mathfrak{R}_0$ (left) and the region in which $\mathfrak{R}_0 > 1$ (right). We plot $\mathfrak{R}_0$ (z-axis) compared to the effectiveness of PIs (x-axis) and RIIs (y-axis). The horizontal plane represents when $\mathfrak{R}_0 = 1$.

Threshold Dynamics

This subsection is devoted to the study of the threshold dynamics of system (4.1). Let

$$\mathbf{X}_0 = \{(T_0, T_0^*, M_0, M_0^*, M_{B0}, M_{B0}^*, V_0, V_{B0}) \in \mathbb{R}_+^8 : T_0^* > 0,\ M_0^* > 0,\ M_{B0}^* > 0,$$

$$V_0 > 0,\ V_{B0} > 0\},$$

and

$$\partial\mathbf{X}_0 := \mathbb{R}_+^8 \backslash \mathbf{X}_0 = \{(T_0, T_0^*, M_0, M_0^*, M_{B0}, M_{B0}^*, V_0, V_{B0}) \in \mathbb{R}_+^8 :$$

$$T_0^* = 0 \text{ or } M_0^* = 0 \text{ or } M_{B0}^* = 0 \text{ or } V_0 = 0 \text{ or } V_{B0} = 0\}.$$

Lemma 3. *Assume that*

$$(T(t), T^*(t), M(t), M^*(t), M_B(t), M_B^*(t), V(t), V_B(t))$$

is a solution of the system (4.1) *with initial value*

$$(T(0), T^*(0), M(0), M^*(0), M_B(0), M_B^*(0), V(0), V_B(0)) \in \mathbf{X}_0.$$

Then

$$(T(t), T^*(t), M(t), M^*(t), M_B(t), M_B^*(t), V(t), V_B(t)) \gg 0, \ \forall \ t > 0.$$

PROOF. In view of the first equation of system (4.1), it follows that

$$T(t) = e^{-\int_0^t b_1(s_1)ds_1} \left[\int_0^t \lambda e^{\int_0^{s_2} b_1(s_1)ds_1} ds_2 + T(0) \right],$$

where

$$b_1(t) := d + \Phi_b \beta V(t).$$

Thus, $T(t) > 0, \ \forall \ t > 0$. From the third equation of system (4.1), it follows that

$$M(t) = e^{-\int_0^t b_2(s_1)ds_1} \left[\int_0^t e^{\int_0^{s_2} b_2(s_1)ds_1} a_2(s_2)ds_2 + M(0) \right],$$

where

$$a_2(t) := \lambda_M + \psi M_B(t) \geq \lambda_M,$$

and

$$b_2(t) := \Phi_b \beta_M V(t) + \varphi + d_M.$$

Thus, $M(t) > 0, \ \forall \ t > 0$. From the fifth equation of system (4.1), it follows that

$$M_B(t) = e^{-\int_0^t b_3(s_1)ds_1} \left[\int_0^t e^{\int_0^{s_2} b_3(s_1)ds_1} a_3(s_2)ds_2 + M_B(0) \right],$$

where

$$a_3(t) := \varphi M(t) > 0,$$

and

$$b_3(t) := \psi + \Phi_{\pi b}\beta_M V_B(t) + d_M \geq \psi + d_M.$$

Thus, $M(t) > 0,\ \forall\ t > 0$. Next, we regard Theorem 4.1.1 of [65] as a generalized version to nonautonomous systems, and the irreducibility of the cooperative matrix

$$\begin{pmatrix} -\delta & 0 & 0 & \Phi_b\beta T(t) & 0 \\ 0 & -(\varphi+\delta_M) & \psi & \Phi_b\beta_M M(t) & 0 \\ 0 & \varphi & -(\psi+\delta_M) & 0 & \Phi_{\pi b}\beta_M M_B(t) \\ \Phi_p p & \Phi_p p_M & 0 & -c & 0 \\ 0 & 0 & \Phi_{\pi p} p_M & 0 & -c \end{pmatrix} \tag{4.11}$$

implies that

$$(T^*(t), M^*(t), M_B^*(t), V(t), V_B(t)) \gg 0,\ \forall\ t > 0.$$

This completes the proof. □

Theorem 2. *The following statements hold.*

(i) If $\mathfrak{R}_0 < 1$, then the disease-free equilibrium E_0 is globally attractive in $\mathbb{R}^8_+$ for (4.1);

(ii) If $\mathfrak{R}_0 > 1$, then system (4.1) is uniformly persistent with respect to $(\mathbf{X}_0, \partial\mathbf{X}_0)$ in the sense that there is a positive constant $\zeta > 0$ such that every solution

$$(T(t), T^*(t), M(t), M^*(t), M_B(t), M_B^*(t), V(t), V_B(t))$$

of (4.1) with

$$(T(0), T^*(0), M(0), M^*(0), M_B(0), M_B^*(0), V(0), V_B(0)) \in \mathbf{X}_0$$

satisfies

$$\liminf_{t\to\infty} u(t) \geq \zeta,\ \forall\ u = T^*,\ M^*,\ M_B^*,\ V,\ V_B. \tag{4.12}$$

Furthermore, system (4.1) *admits at least one (componentwise) positive equilibrium.*

PROOF. Part (i). Assume that $\mathfrak{R}_0 < 1$. It then follows from Lemma 2 (iii) that $s(J) < 0$. Thus, there exists a sufficiently small positive number ρ_0 such that $s(J_{\rho_0}) < 0$ (see, e.g., [38, Section II.5.8]), where

$$J_{\rho_0} = \begin{pmatrix} -\delta & 0 & 0 & \Phi_b\beta(\hat{T}+\rho_0) & 0 \\ 0 & -(\varphi+\delta_M) & \psi & \Phi_b\beta_M(\hat{M}+\rho_0) & 0 \\ 0 & \varphi & -(\psi+\delta_M) & 0 & \Phi_{\pi b}\beta_M(\hat{M}_B+\rho_0) \\ \Phi_p p & \Phi_p p_M & 0 & -c & 0 \\ 0 & 0 & \Phi_{\pi p}p_M & 0 & -c \end{pmatrix}$$

has non-negative off-diagonal elements, and J_{ρ_0} is irreducible. From the first, third, and fifth equations of system (4.1), together with positivity of solutions, it follows that

$$\frac{dT}{dt} \leq \lambda - dT, \tag{4.13}$$

and

$$\begin{cases} \frac{dM}{dt} \leq \lambda_M - (\varphi + d_M)M + \psi M_B, \\ \frac{dM_B}{dt} \leq \varphi M - (\psi + d_M)M_B. \end{cases} \tag{4.14}$$

By the comparison principle and Lemma 1, we see that

$$\limsup_{t\to\infty} T(t) \leq \hat{T},\ \limsup_{t\to\infty}(M(t), M_B(t)) \leq (\hat{M}, \hat{M}_B).$$

It follows that there is a $t_1 > 0$ such that

$$T(t) \le \hat{T} + \rho_0,\ M(t) \le \hat{M} + \rho_0,\ M_B(t) \le \hat{M}_B + \rho_0,\ \forall\ t \ge t_1. \tag{4.15}$$

In view of (4.15) and system (4.1), we see that

$$\begin{cases} \frac{dT^*}{dt} \le \Phi_b\beta(\hat{T} + \rho_0)V - \delta T^*,\ \forall\ t \ge t_1, \\ \frac{dM^*}{dt} \le \Phi_b\beta_M(\hat{M} + \rho_0)V + \psi M_B^* - (\varphi + \delta_M)M^*,\ \forall\ t \ge t_1, \\ \frac{dM_B^*}{dt} \le \Phi_{\pi b}\beta_M(\hat{M}_B + \rho_0)V_B + \varphi M^* - (\psi + \delta_M)M_B^*,\ \forall\ t \ge t_1, \\ \frac{dV}{dt} = \Phi_p p T^* + \Phi_p p_M M^* - cV,\ \forall\ t \ge t_1, \\ \frac{dV_B}{dt} = \Phi_{\pi p} p_M M_B^* - cV_B,\ \forall\ t \ge t_1. \end{cases} \tag{4.16}$$

Consider the following auxiliary system

$$\begin{cases} \frac{dT^*}{dt} = \Phi_b\beta(\hat{T} + \rho_0)V - \delta T^*,\ \forall\ t \ge t_1, \\ \frac{dM^*}{dt} = \Phi_b\beta_M(\hat{M} + \rho_0)V + \psi M_B^* - (\varphi + \delta_M)M^*,\ \forall\ t \ge t_1, \\ \frac{dM_B^*}{dt} = \Phi_{\pi b}\beta_M(\hat{M}_B + \rho_0)V_B + \varphi M^* - (\psi + \delta_M)M_B^*,\ \forall\ t \ge t_1, \\ \frac{dV}{dt} = \Phi_p p T^* + \Phi_p p_M M^* - cV,\ \forall\ t \ge t_1, \\ \frac{dV_B}{dt} = \Phi_{\pi p} p_M M_B^* - cV_B,\ \forall\ t \ge t_1. \end{cases} \tag{4.17}$$

Since J_{ρ_0} has non-negative off-diagonal elements and J_{ρ_0} is irreducible, it follows that $s(J_{\rho_0})$ is simple and associates a strongly positive eigenvector $\tilde{v} \in \mathbb{R}^5$ (see, e.g., [66, Theorem A.5]). For any solution $(T(t), T^*(t), M(t), M^*(t), M_B(t), M_B^*(t), V(t), V_B(t))$ of (4.1) with nonnegative initial value

$$(T(0), T^*(0), M(0), M^*(0), M_B(0), M_B^*(0), V(0), V_B(0)),$$

there is a sufficiently large $b > 0$ such that

$$(T^*(t_1), M^*(t_1), M_B^*(t_1), V(t_1), V_B(t_1)) \leq b\tilde{v}$$

holds. It is easy to see that $U(t) := be^{s(J^0_{\rho_0})(t-t_1)}\tilde{v}$ is a solution of (4.17) with $U(t_1) := b\tilde{v}$. By the comparison principle [66, Theorem B.1], it follows that

$$(T^*(t), M^*(t), M_B^*(t), V(t), V_B(t)) \leq be^{s(J_{\rho_0})(t-t_1)}\tilde{v},\ \forall\ t \geq t_1.$$

Since $s(J_{\rho_0}) < 0$, it follows that

$$\lim_{t\to\infty}(T^*(t), M^*(t), M_B^*(t), V(t), V_B(t)) = (0, 0, 0, 0, 0).$$

It then follows that the equations for $T(t)$ and $(M(t), M_B(t))$ in (4.1) are asymptotic to (4.4) and (4.5), respectively. By the theory for asymptotically autonomous semiflows (see, e.g., [70, Corollary 4.3]) and Lemma 1, it follows that

$$\lim_{t\to\infty} T(t) = \hat{T},\ \lim_{t\to\infty}(M(t), M_B(t)) = (\hat{M}, \hat{M}_B).$$

Part (i) is proved.

Part (ii). Assume that $\mathfrak{R}_0 > 1$. It then follows from Lemma 2 (ii) that $s(J) > 0$. Suppose $\Pi(t)P$ is the solution maps generated by system (4.1) with initial value P. By Theorem 1, we see that system $\{\Pi(t)\}_{t\geq 0}$ admits a global attractor in $\mathbb{R}^8_+$. Now we prove that $\{\Pi(t)\}_{t\geq 0}$ is uniformly persistent with respect to $(\mathbf{X}_0, \partial\mathbf{X}_0)$. By Lemma 3, it follows that both $\mathbb{R}^8_+$ and $\mathbf{X}_0$ are positively invariant. Clearly, $\partial\mathbf{X}_0$ is relatively closed in $\mathbb{R}^8_+$.

Let $M_\partial := \{P \in \partial\mathbf{X}_0 : \Pi(t)P \in \partial\mathbf{X}_0,\ \forall\ t \geq 0\}$ and $\omega(P)$ be the omega limit set of the orbit $O^+(P) := \{\Pi(t)P : t \geq 0\}$. We next prove the following claims.

Claim 1: $\omega(P) = \{E_0\},\ \forall\ P \in M_\partial$.

Since $P \in M_\partial$, we have $\Pi(t)P \in M_\partial,\ \forall\ t \geq 0$. Next, we show that

$$(T^*(t), M^*(t), M_B^*(t), V(t), V_B(t)) = (0, 0, 0, 0, 0),\ \forall\ t > 0. \tag{4.18}$$

Assume that (4.18) is not true. Then there exists $\tau_0 > 0$ such that

$$(T^*(\tau_0), M^*(\tau_0), M_B^*(\tau_0), V(\tau_0), V_B(\tau_0)) \neq (0, 0, 0, 0, 0).$$

Then the irreducibility of the cooperative matrix (4.11) implies that

$$(T^*(t), M^*(t), M_B^*(t), V(t), V_B(t)) \gg 0,\ \forall\ t > \tau_0,$$

which contradicts the fact that $\Pi(t)P \in M_\partial,\ \forall\ t \geq 0$, and hence, (4.18) is true. By (4.18), it follows that the equations for $T(t)$ and $(M(t), M_B(t))$ in (4.1) satisfies (4.4) and (4.5), respectively. By Lemma 1, it follows that

$$\lim_{t\to\infty} T(t) = \hat{T},\ \lim_{t\to\infty}(M(t), M_B(t)) = (\hat{M}, \hat{M}_B).$$

Claim 1 is proved.

Since $s(J) > 0$, there exists a sufficiently small positive number σ_0 such that $s(J_{\sigma_0}) > 0$ (see, e.g., [38, Section II.5.8]), where

$$J_{\sigma_0} = \begin{pmatrix} -\delta & 0 & 0 & \Phi_b\beta(\hat{T} - \sigma_0) & 0 \\ 0 & -(\varphi + \delta_M) & \psi & \Phi_b\beta_M(\hat{M} - \sigma_0) & 0 \\ 0 & \varphi & -(\psi + \delta_M) & 0 & \Phi_{\pi b}\beta_M(\hat{M}_B - \sigma_0) \\ \Phi_p p & \Phi_p p_M & 0 & -c & 0 \\ 0 & 0 & \Phi_{\pi p} p_M & 0 & -c \end{pmatrix}$$

has non-negative off-diagonal elements and J_{σ_0} is irreducible.

Claim 2: E_0 is a uniform weak repeller for $\Pi(t)$ in the sense that

$$\limsup_{t\to\infty} \|\Pi(t)P - E_0\| \geq \sigma_0,\ \forall\ P \in \mathbf{X}_0.$$

Suppose, by contradiction, there exists $P_0 \in \mathbf{X}_0$ such that

$$\limsup_{t\to\infty} \|\Pi(t)P_0 - E_0\| < \sigma_0.$$

Thus, there exists $t_2 > 0$ such that

$$T(t) \geq \hat{T} - \sigma_0,\ M(t) \geq \hat{M} - \sigma_0,\ M_B(t) \geq \hat{M}_B - \sigma_0,\ \forall\ t \geq t_2. \tag{4.19}$$

In view of (4.19) and system (4.1), we see that

$$\begin{cases} \frac{dT^*}{dt} \geq \Phi_b\beta(\hat{T} - \sigma_0)V - \delta T^*,\ \forall\ t \geq t_2, \\ \frac{dM^*}{dt} \geq \Phi_b\beta_M(\hat{M} - \sigma_0)V + \psi M_B^* - (\varphi + \delta_M)M^*,\ \forall\ t \geq t_2, \\ \frac{dM_B^*}{dt} \geq \Phi_{\pi b}\beta_M(\hat{M}_B - \sigma_0)V_B + \varphi M^* - (\psi + \delta_M)M_B^*,\ \forall\ t \geq t_2, \\ \frac{dV}{dt} = \Phi_p p T^* + \Phi_p p_M M^* - cV,\ \forall\ t \geq t_2, \\ \frac{dV_B}{dt} = \Phi_{\pi p} p_M M_B^* - cV_B,\ \forall\ t \geq t_2. \end{cases} \tag{4.20}$$

Consider the following auxiliary system

$$\begin{cases} \frac{dT^*}{dt} = \Phi_b\beta(\hat{T} - \sigma_0)V - \delta T^*,\ \forall\ t \geq t_2, \\ \frac{dM^*}{dt} = \Phi_b\beta_M(\hat{M} - \sigma_0)V + \psi M_B^* - (\varphi + \delta_M)M^*,\ \forall\ t \geq t_2, \\ \frac{dM_B^*}{dt} = \Phi_{\pi b}\beta_M(\hat{M}_B - \sigma_0)V_B + \varphi M^* - (\psi + \delta_M)M_B^*,\ \forall\ t \geq t_2, \\ \frac{dV}{dt} = \Phi_p p T^* + \Phi_p p_M M^* - cV,\ \forall\ t \geq t_2, \\ \frac{dV_B}{dt} = \Phi_{\pi p} p_M M_B^* - cV_B,\ \forall\ t \geq t_2. \end{cases} \tag{4.21}$$

Since J_{σ_0} is irreducible and has non-negative off-diagonal elements, it follows that

$s(J_{\sigma_0})$ is simple and associates a strongly positive eigenvector $\tilde{u} \in \mathbb{R}^5$(see, e.g., [66, Theorem A.5]). By Lemma 3, it follows that

$$(T^*(t_2), M^*(t_2), M_B^*(t_2), V(t_2), V_B(t_2)) \gg 0.$$

Thus, there is a positive number $\varsigma > 0$ such that

$$(T^*(t_2), M^*(t_2), M_B^*(t_2), V(t_2), V_B(t_2)) \geq \varsigma\tilde{u}$$

holds. It is easy to see that $W(t) := \varsigma e^{s(J_{\sigma_0})(t-t_2)}\tilde{u}$ is a solution of (4.21) with $W(t_2) := \varsigma\tilde{u}$. By the comparison principle [66, Theorem B.1], it follows that

$$(T^*(t), M^*(t), M_B^*(t), V(t), V_B(t)) \geq \varsigma e^{s(J_{\sigma_0})(t-t_2)}\tilde{u},\ \forall\ t \geq t_2.$$

Since $s(J_{\sigma_0}) > 0$, it follows that

$$\lim_{t\to\infty} T^*(t) = \lim_{t\to\infty} M^*(t) = \lim_{t\to\infty} M_B^*(t) = \lim_{t\to\infty} V(t) = \lim_{t\to\infty} V_B(t) = \infty.$$

This contradiction proves the claim 2.

From the above claims, it follows that any forward orbit of $\Pi(t)$ in M_∂ converges to E_0 which is isolated in $\mathbb{R}^8_+$ and $W^s(E_0) \cap \mathbf{X}_0 = \emptyset$, where $W^s(E_0)$ is the stable set of E_0 (see [64]). It is obvious that there is no cycle in M_∂ from E_0 to E_0. By [71, Theorem 4.6] (see also [82, Theorem 1.3.1] and [33, Theorem 4.3 and Remark 4.3]), we conclude that system (4.1) is uniformly persistent with respect to $(\mathbf{X}_0, \partial\mathbf{X}_0)$ in the sense that there is a positive constant $\zeta > 0$ such that (4.12) holds.

By [81, Theorem 2.4] (see also [82, Theorem 1.3.7]), system (4.1) has at least one equilibrium

$$(\check{T}, \check{T}^*, \check{M}, \check{M}^*, \check{M}_B, \check{M}_B^*, \check{V}, \check{V}_B) \in \mathbf{X}_0,$$

and hence, $\check{T}^* > 0,\ \check{M}^* > 0,\ \check{M}_B^* > 0,\ \check{V} > 0$, and $\check{V}_B > 0$. Furthermore, we see that

$$\check{T} = \frac{\lambda}{\Phi_b \beta \check{V} + d},$$

and $(\check{M}, \check{M}_B)$ satisfies

$$\begin{cases} \lambda_M - \Phi_b \beta_M \check{V} M - \varphi M + \psi M_B - d_M M = 0, \\ \varphi M - \psi M_B - \Phi_{\pi b} \beta_M \check{V}_B M_B - d_M M_B = 0, \end{cases} \tag{4.22}$$

From (4.22), it is not hard to see that $\check{M} > 0$ and $\check{M}_B > 0$. Thus,

$$(\check{T}, \check{T}^*, \check{M}, \check{M}^*, \check{M}_B, \check{M}_B^*, \check{V}, \check{V}_B)$$

is a (componentwise) positive equilibrium of system (4.1). This completes the proof of Part (ii). □

Numerical Simulations

In the following sections we show the numerical simulations of the plasma viral load (PVL) and the brain viral load (BVL) under different treatment protocols. We consider how the different protocols affect the time the viral loads take to reach undetectable levels. We first examine whether the CPE score reduces treatment time in the plasma and what effect it has on the reduction time for the brain viral load. Next, we explore how the slope of the dose-response curve affects the date of viral undetectability. Then, we analyze the effect of larger numbers of drugs in a given ART regimen, and finally we examine if the initial treatment day affects the average day the PVL and BVL clear below measurable levels. For all simulations we consider a detected viral load to be fifty copies of viral RNA per μL, which is the standard

lower limit to measure HIV according to current assays [1].

Effect of the CPE Score

To better understand the effect of the CPE score on the overall treatment of HIV, we considered its effect on the time that the PVL and the BVL reduce to undetected levels in the presence of constant treatment. In Figure 17 we show the average time the viral loads in the brain and the plasma take to become undetectable depending on the CPE score of an ART regimen with a single drug. Treatment was assumed to begin after a steady-state viral load was achieved ($\sim$250 dpi) and we considered a single RTI and a single PI.

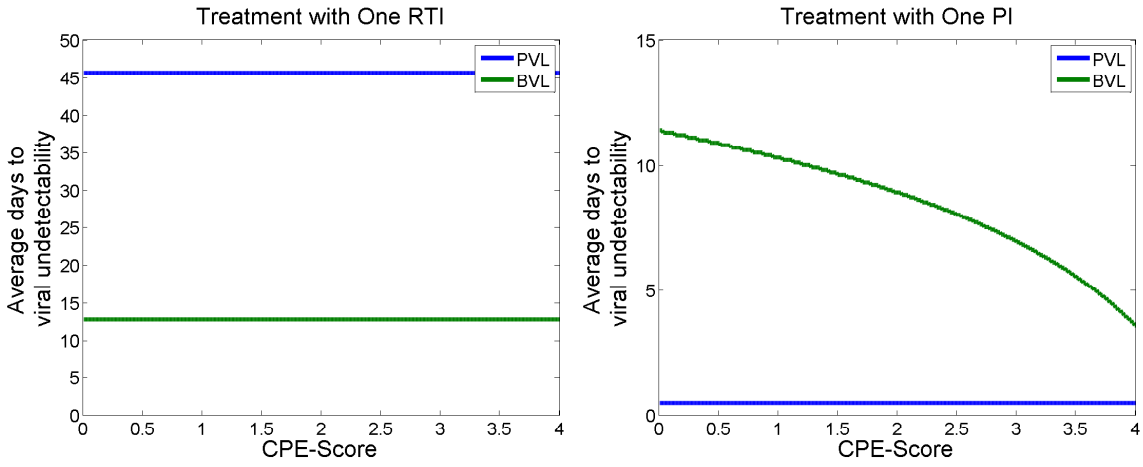

Figure 17: The average time the viral loads in the plasma (blue) and the brain (green) become undetectable depending on the mean CPE score of the ART regimen with either a single RTI (left) or PI (right).

We clearly observe that the CPE score has no effect on the plasma viral load, as the average number of days for the PVL to become undetectable remains constant despite the CPE score or the drug type (RTI or PI). However, even with one drug present, we observe that the CPE score affects the number of days to viral undetectability for a PI differently than it does for an RTI. In particular, as the CPE score increases for a PI, the number of days for the BVL to reach undetectable levels decrease ($\approx$ 10 days to $\approx$ 3 days). There is no observed effect of the CPE score on the BVL if an ART protocol includes a only a single RTI. Hence, the BBB affects single-drug protocols with PIs more than RTIs.

To analyze this effect further we considered ART with two drugs. We present the model simulations of the number of days to viral undetectability in the PVL and BVL in Figure 18. Treatment was initiated after steady-state infection had occurred (250 dpi) and we considered two PIs, 2 RTIs, and a combination of one PI and one RTI.

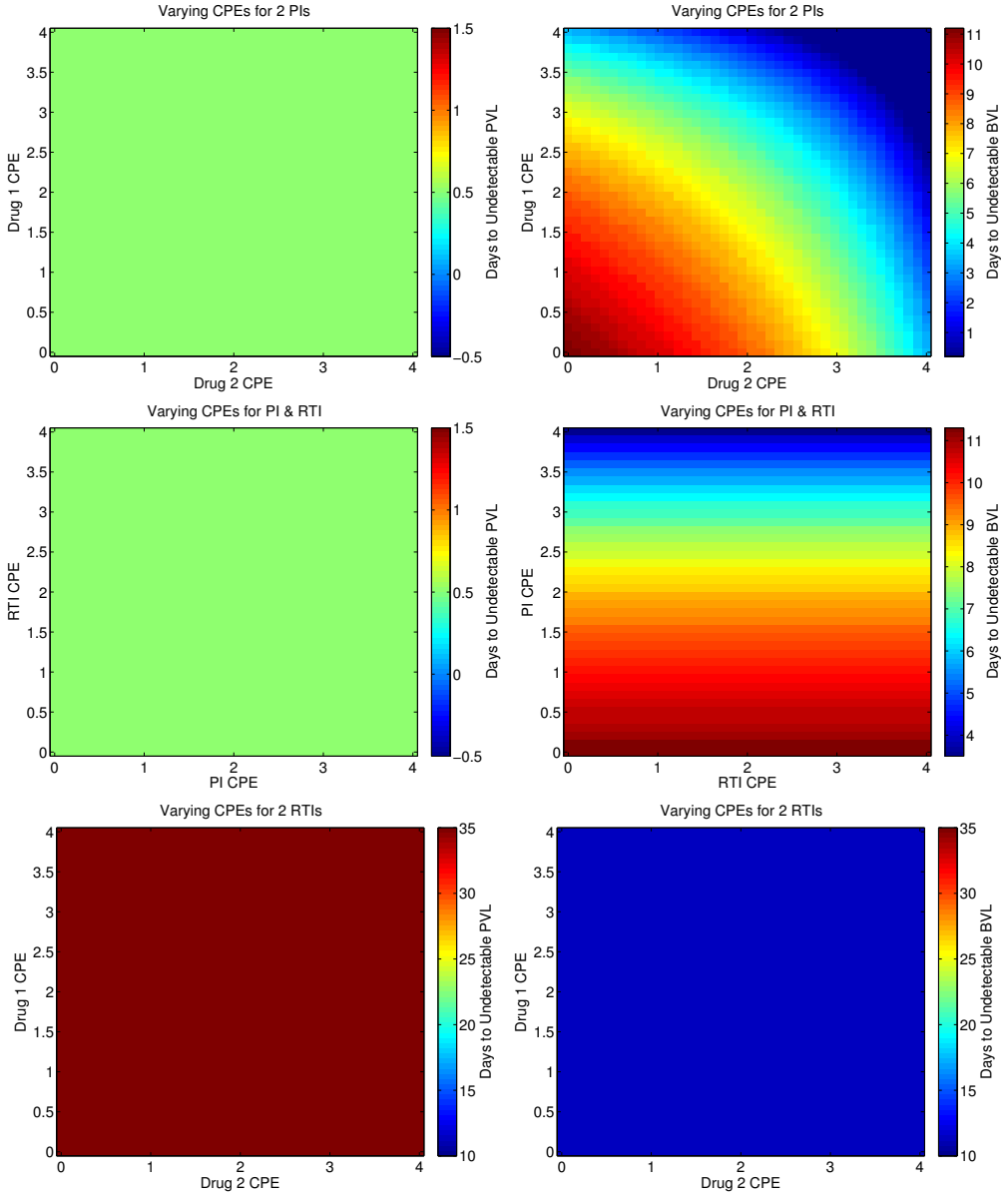

Figure 18: Average days to viral undetectability in the PVL (left column) and BVL (right column) depending on the CPE scores for two PIs (top row), two RTIs (bottom row) and one RTI and one PI (middle row).

Similar to the treatments with a single drug we see no discernible effect of the CPE score on the PVL with two drugs. However, we observe a strong effect of the CPE score on the days for the BVL to become undetectable in the presence of constant treatment with two drugs. For ART with two PIs we observe that as CPE increases for either drug, the days for the virus to become undetected decreases (≈ 9 days v. ≈ 1 day). Furthermore, if ART includes an RTI and a PI we note that as the CPE score increase for the PI, the days to an undetectable BVL decreases, however the CPE score for the RTI shows no effect on the days to undetectability in the BVL. In fact, if treatment includes only two RTIs we do not observe an effect of the CPE score on the overall time to viral undetectability. This suggests that protease inhibitors with higher CPE scores should be considered more than RTIs to better control HIV in the brain.

Effect of the Slope of the dose-response Curve

Since the CPE score was more effective for PIs, which generally possess higher slopes of the dose-response curve than RTIs, in this section we used our model (4.1) to explore the influence of the slope of the dose-response curve on the date viral RNA becomes undetectable. We first considered constant treatment with exactly one drug. In Figure 19 we plotted the average date the virus in the plasma and the brain takes to become undetectable depending on the slope of the dose-response curve. Treatment was set to begin after a steady-state viral load was achieved in the brain and the plasma (250 dpi), and we varied slopes between zero and 5. As per experimental evidence [61], we considered any drug whose slope, m, is greater than 1.9 to be a protease inhibitor, and a drug with $m \leq 1.9$ is considered to be an RTI (see Table 4).

A single-drug ART protocol was considered with a low CPE score and a high CPE score (CPE$= 1$ vs. CPE$= 4$).

We observe that if $m \leq 1.9$ (RTI) then the PVL becomes undetectable after at least 40 days, whereas if $m > 1.9$ (PI) then the PVL reaches undetectable levels within a single day. The number of days the BVL takes to reach undetectable levels also decreases as the slope of the dose-response curve increases, however this reduction is significantly less than that observed in the PVL (≈ 40 days less compared to ≈ 6 days less). Interestingly, for low slopes corresponding to an RTI, we note that the PVL becomes undetectable several weeks after the BVL becomes undetectable, and that this behavior switches for the slope corresponding to a protease inhibitor. This switch occurs regardless of the CPE score of the drug, reinforcing the observation from the previous section that RTIs are less effective against the PVL.

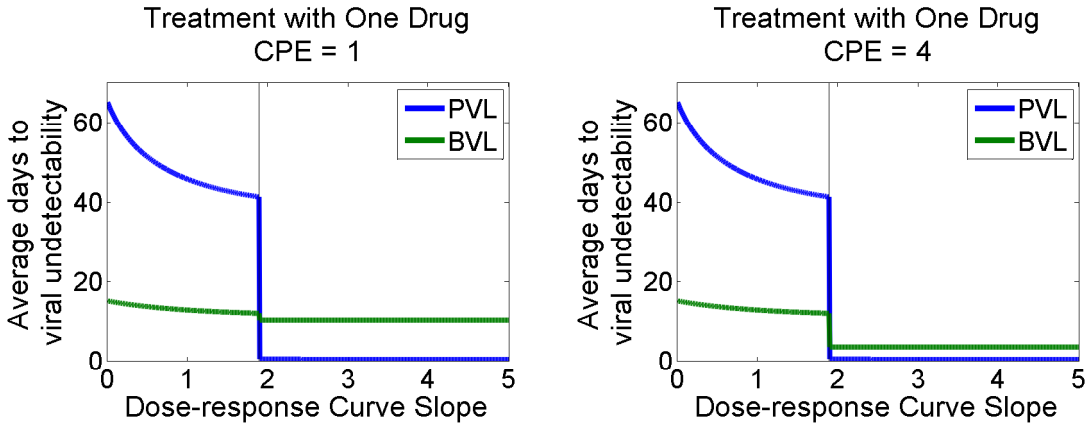

Figure 19: Model simulations of the total time it takes the viral load in the plasma to become undetectable depending on the slope of the dose-response curve. If the slope, m, was greater than 1.9 that drug was taken to be a PI, whereas if $m \leq 1.9$ we considered that drug an RTI.

To examine the effect of the dose-response curve slope further we considered ART that included both an RTI and a PI. RTIs and PIs were considered with high and low CPE scores each and we predicted the total days to viral undetectability in the PVL and the BVL in Figures 20 and 21, respectively. We note that in all cases the BVL and the PVL measured little to no difference in the number of days before they become undetectable, suggesting that once multiple drugs are present in ART, the slope of the dose-response curve does not change the total number of days to viral undetectability. However, for ART with two drugs, even if the slopes of the dose-response curves are low, the average number of days to viral undetectability is much less (≈ 10 days compared to ≈ 40 days). In particular we observe that if both

an RTI and a PI are present in ART, the BVL reaches undetected levels at least three days after the PVL becomes undetectable.

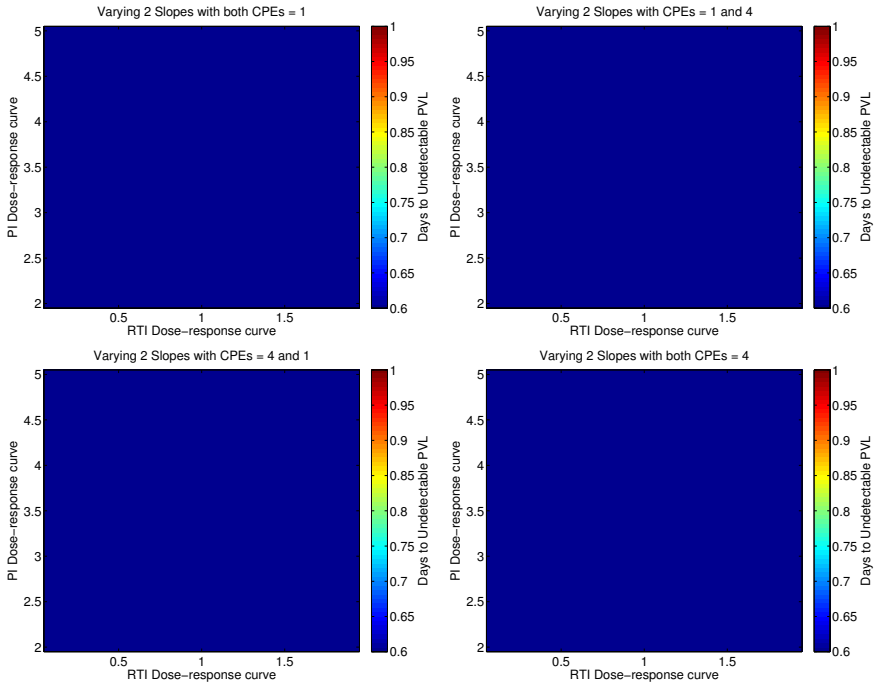

Figure 20: The total days to viral undetectability in the PVL depending on the slopes of the dose-response curve of both an RTI and a PI. PIs with a CPE score of one (top row) and four (bottom row) were considered with RTIs with a CPE score of one (left column) and four (right column).

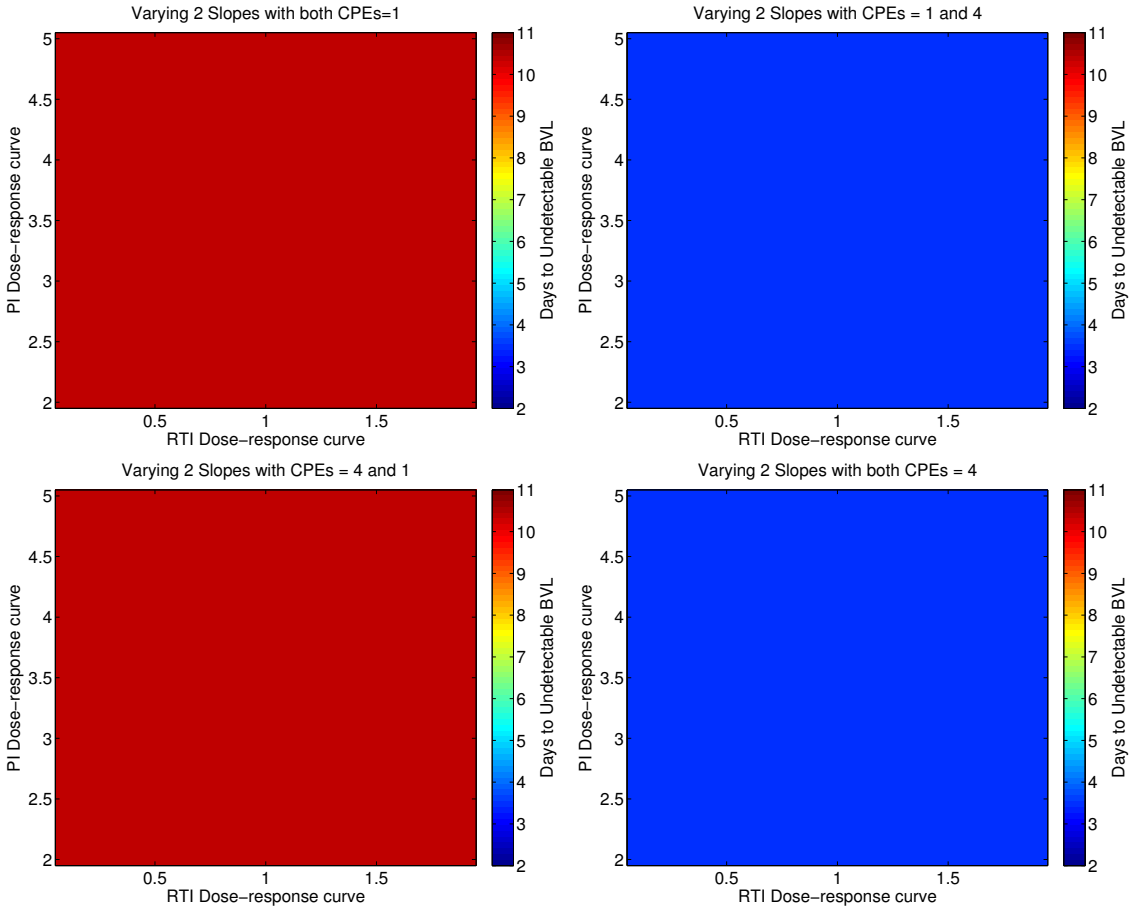

Figure 21: The total days to viral undetectability in the PVL depending on the slopes of the dose-response curve of both an RTI and a PI. PIs with a CPE score of one (top row) and four (bottom row) were considered with RTIs with a CPE score of one (left column) and four (right column).

Table 3: Fixed parameters for all monkeys, arithmetic mean data, median data, and geometric mean data.

Model Values			
Initial Values			
Name	Symbol	Value	Source
Initial uninfected T-cells	T_0	38700	Vaidya *et al.* [73]
Initial infected T-cells	T_0^*	0	Kumar *et al.* [45]
Initial uninfected plasma Macrophages	M_0	1463000	Haney *et al.* [30]
Initial infected plasma Macrophages	M_0^*	0	Kumar *et al.* [45]
Initial uninfected CSF Macrophages	M_{B0}	20000	Haney *et al.* [30]
Initial infected CSF Macrophages	M_{B0}	0	Kumar *et al.* [45]
Initial plasma free Virions	V_0	200	Kumar *et al.* [45]
Initial CSF free Virions	V_{B0}	0	Kumar *et al.* [45]
Parameter Values			
Name	Symbol	Value	Source
Death rate for uninfected T-cells	d	0.01 (day^{-1})	Stafford *et al.* [67]
Death rate for uninfected Macrophages	d_M	0.00185 (day^{-1})	Prinz *et al.* [53]
Recruitment rate for T-cells	λ	387 (day^{-1})	Calculated
Recruitment rate for Macrophages	λ_M	2743.55 (day^{-1})	Calculated
Viral production from infected T-cells	p	50000 (day^{-1})	Chen *et al.* [16]
Viral production from infected macrophages	p_M	1000 (day^{-1})	Schwartz *et al.* [60]
Viral clearance rate	c	23 (day^{-1})	Ramratnam *et al.* [54]
T-cell infection rate	β	3.5830E-8 (ml/day)	Estimated
Death rate for infected T-cells	δ	1.4551 (day^{-1})	Estimated
Macrophage infection rate	β_M	8.653E-10 (ml/day)	Estimated
Death rate for infected macrophages	δ_M	0.2060 (day^{-1})	Estimated
Rate of macrophage entry into the brain	φ	0.03876 (day^{-1})	Estimated
Rate of macrophage exit from the brain	ψ	8.9953 (day^{-1})	Estimated

Table 4: Chart of drugs Emacs score and CPE scores.

Drug Type	Drug Name	Drug Abbreviation	Drug CPE Score (according to Letendre, 2011 [46])	Inhibitory Quotient (Davg/IC50)	Hill's coefficient m_i	Φ_j	ε_j
NRTI	Abacavir	ABC	3	50.9	0.95	0.023353685	0.976646315
	Didanosine	ddI	2	2.4	1.07	0.281556981	0.718443019
	Emtricitabine	FTC	3	226.9	1.18	0.001657276	0.998342724
	Lamivudine	3TC	2	101.4	1.15	0.004908169	0.995091831
	Stavudine	d4T	2	0.85	1.13	0.545782997	0.454217003
	Tenofovir	TDF	1	2.7	0.97	0.276187136	0.723812864
	Zalcitabine	ddC	1	Not included	Not included	Not calculated	not calculated
	Zidovudine	AZT	4	2.4	0.85	0.322097664	0.677902336
NNRTI	Delavirdine	DLV	3	101.2	1.56	0.000744038	0.999255962
	Efavirenz	EFV	3	1042.5	1.69	7.93319E-6	0.999992067
	Etravirine	TMC125	2	203.4	1.81	6.63523E-5	0.999933648
	Nevirapine	NVP	4	195.6	1.55	0.000280709	0.99719291
	Atazanavir	ATV	2	199.8	2.69	6.47736E-7	0.999999352
PI	Darunavir/r	DRV	3	410.6	3.61	3.67754E-10	1
	Fosamprenavir	APV	2	39.7	2.09	0.000455334	0.999544666
	Indinavir	IDV	3	60	4.53	8.80998E-9	0.999999991
	Lopinavir/r	LPV	3	343.2	2.05	6.34053E-6	0.999993659
	Nelfinavir	NFV	1	21.5	1.81	0.003860172	0.996139828
	Saquinavir	SQV	1	120	3.65	2.57625E-8	0.999999974
	Tipranavir/r	tPV	1	244.5	2.51	1.01256E-6	0.999998987
FI	Enfuvirtide	T20	1	25.1	1.65	0.004879933	0.995120067
II	Raltegravir	RAL	3	89.8	1.1	0.007052165	0.992947835

Effect of Multiple Drugs

In the previous section our model predictions showed that more drugs in a cART regimen led to less time for the virus to become undetectable. However, it is unclear whether this correlation is stronger for the brain or for the plasma. To better understand this we examined the effect of ART with three or more drugs on the days to viral undetectability in the CSF and the plasma. Random slopes between 0 and 5 were taken and paired with random CPE scores between 0 and 5. Drug types were categorized by the slope of the dose-response curve (RTI if $m \leq 1.9$, PI if $m > 1.9$). Treatment was assumed to be constant and initiated after the viral loads reached a steady-state (≈ 250 dpi). In Figure 22 we present the boxplots of the days for the PVL and BVL to reach undetectable levels after simulations of 15,000 random drug combinations of at least three drugs.

In all cases we observe that ART with multiple drugs reduces the PVL to undetectable levels before the BVL becomes undetectable. However, we note about a large number of outliers among the PVL implying some uncertainties. This is likely because we chose uniformly distributed random slopes between 0 and 5, which has a greater likelihood of selecting slopes corresponding to PIs ($m > 1.9$).

We note that the number of drugs in a treatment protocol affects the reduction time of the BVL. Specifically, the median days for the BVL to become undetectible decreases (≈ 7 dpi v. ≈ 0.5 dpi) as the number of drugs in a treatment protocol increases from three to five. We also observe that for drug regimens with a higher number of drugs, viral suppression in the plasma may not indicate viral suppression in the brain. This implies that the BBB potentially poses a stronger effect on multiple

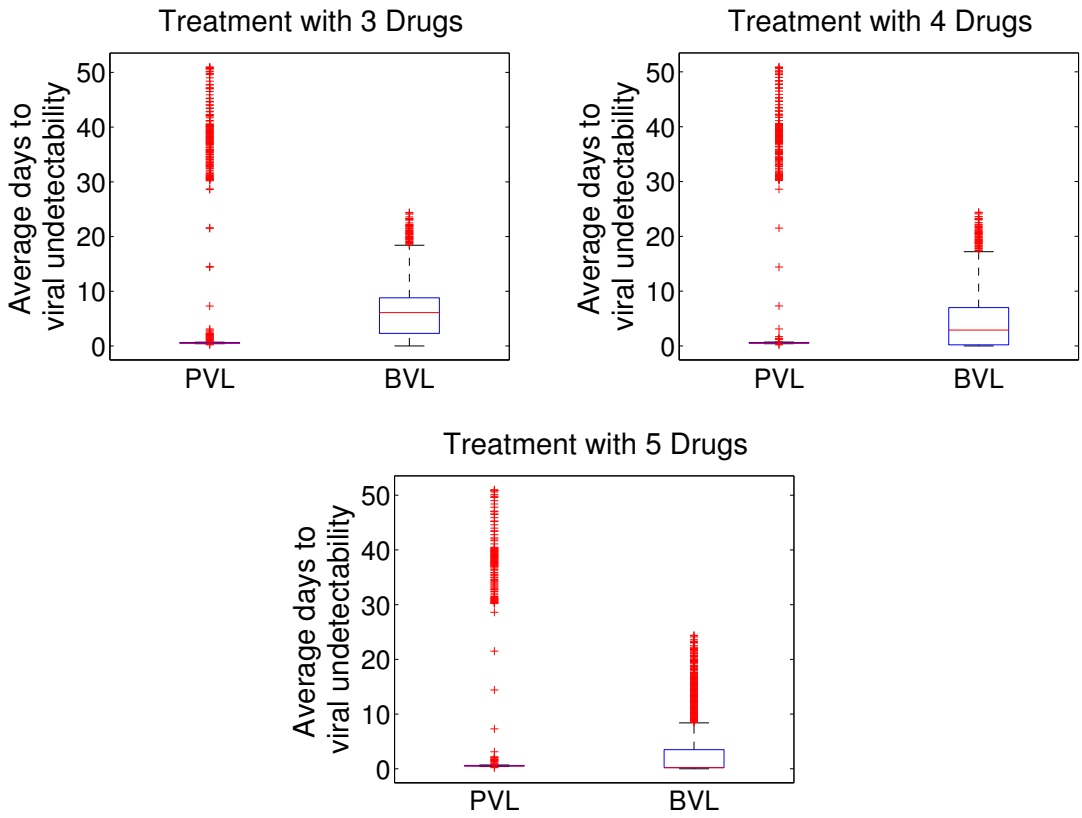

Figure 22: Mean time for the virus to become undetectable (in days) depending on the number of drugs in an ART regimen.

drugs protocols than on smaller combinations of ART.

Effect of Treatment Initiation Time

In Figure 23 we present the predicted time in days post-infection that the plasma viral load and the brain viral load achieve undetectable levels depending on the initial time of treatment. Treatment was assumed to be constant and includes a single RTI or PI with a corresponding CPE score of either one or four. The time of

treatment initiation varied between one and 300 days post-infection (dpi).

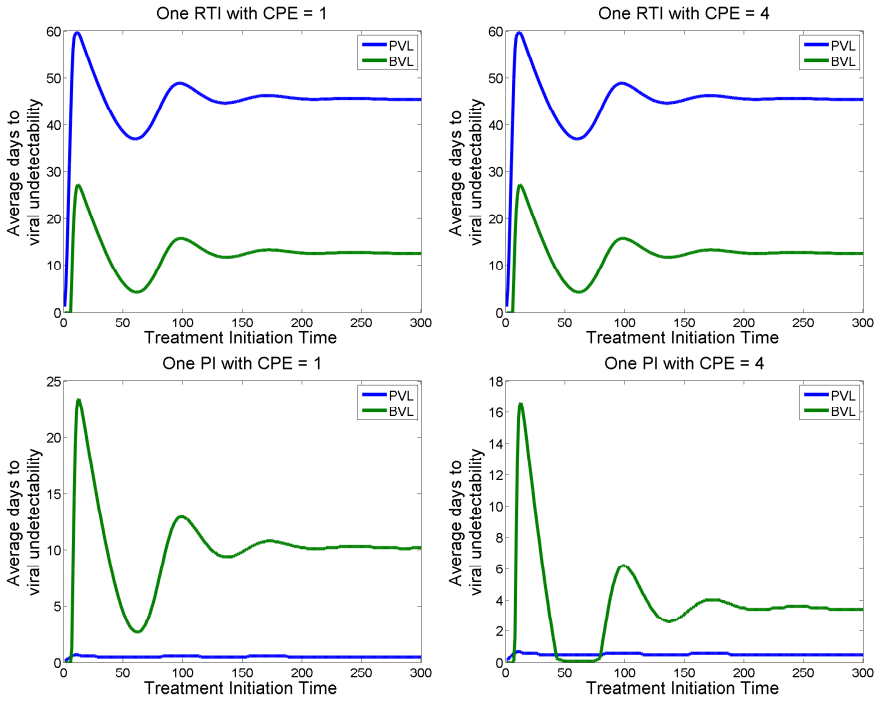

Figure 23: The average time (in days) it takes for viral RNA copies to become undetectable (< 50 copies per μL [1]) in the plasma (blue) and the brain (green) in the presence of constant treatment from one RTI (top row) or from a PI (bottom row) with a low CPE score (left column) and high CPE score (right column), depending on the initial date of treatment.

We observe that if treatment does not begin after steady-state infection, it is clear that the earliest initiated treatment (< 3 dpi) is ideal as it can prevent infection from reach detectable levels in the brain. This is consistent with previous studies

[17, 75]. Furthermore, our simulations suggest that outside of early treatment, in general, the time for the PVL and BVL to reach undetectable levels varies significantly within the first 100 days post-infection. For instance, if treatment begins during the second week post-infection we observe that the virus is detectable in both the plasma and the brain for longer ($15 - 20$ dpi) than for any other initial treatment time. If constant ART is initiated between eight and ten weeks post-infection, the total time before viral undetectability is significantly less than any other time of treatment initiation (<5 dpi in the brain, ≈ 8 dpi in the plasma). Treatment initiation after a viral steady-state has been achieved were not observed to significantly affect the time for the virus to attain undetectable levels.

When we compare ART with PIs and RTIs by varying the time of treatment initiation we observe similar dynamics from the previous sections. Specifically, we note that treatment with a PI is extremely effective at reducing the PVL, but less effective at reducing the BVL, whereas ART with an RTI reduces the BVL consistently more efficiently than the PVL. We note that in some cases if the CPE score is high then the time of treatment initiation affects whether the BVL or PVL becomes undetectable first. We do not observe this behavior when varying treatment initiation time for drugs associated with low CPE scores.

CHAPTER 5

STOCHASTIC MODEL OF HIV INFECTION IN THE BRAIN

In this chapter we develop a stochastic model to analyze stochastic effects on the viral dynamics of HIV-1 in the brain. We also compare the predictions of our model to those of our deterministic model. We then examine the computed reaction propensity functions which indicate likely infection behavior. Furthermore, we analyze the overall probability distributions during the most likely infection time predicted by our model.

Introduction

The models developed in chapters 3 and 4 are deterministic models to study the effect of the brain on the comprehensive viral dynamics of HIV-1. Both models illustrated some uncertainty. This uncertainty and the randomness found in biological events suggested a need to develop stochastic model of HIV-1 in the brain. Many stochastic models have been developed to study HIV [80, 20, 37, 47, 52, 69, 72], but these focus on early viral dynamics within the plasma. None consider the brain in their models. There is clearly a need to examine the stochastic effect of the BBB on the viral dynamics of HIV in the brain.

Model Development

Choice of stochastic modeling technique

There are several methods for deriving a stochastic model from a deterministic one. Some of the earliest numerical approximation methods were introduced by Gillespie in 2001 [25], and improved upon later by introducing a faster method for simulations. Methods used to study HIV-1 stochastically range from introducing a random perturbation into any number of parameters [20], complex networking [62], and most commonly a drift function proposed by Allen *et al.* [80]. For any of the latter methods one must prove the non-negativity of the solutions. However, it was observed by Cresson and Sonner [19] that there are some characteristics of deterministic models that cannot be proven to achieve full non-negativity of solutions. In particular, from the system (3.1) we observe that the interaction function

$$\frac{\mathrm{d}}{\mathrm{d}T} = \lambda - \beta VT - dT,$$

contains a constant term. It follows from Corollary 3.1 of [19] that any stochastic model derived from this system using the method in [80] fails to preserve non-negativity. Thus, we attempted the algorithm defined in [25], but due to the large volume of cells in the macrophage population we observed extremely small time-steps, demanding too large a computer cost for practical use. In order to capture the nearest approximate biological phenomenon, we used the τ-leap method from [15] which uses Poisson random variables to approximate large enough time-steps for a 100 day simulation to occur in a reasonable computation time.

Stochastic Model

To formulate the stochastic model we represent each cell and virus compartments from the deterministic model described in Chapter 3 as a continuous random variable. We then let $\vec{\mathbf{X}} = [T, T^*, M, M^*, M_B, M_B^*, V, V_B]^{tr}$ be a continuous random vector such that for a sufficiently small change in time (Δt), the possible state changes, $\Delta\vec{\mathbf{X}} = \vec{\mathbf{X}}(t + \Delta t) - \vec{\mathbf{X}}(t)$, are based on the deterministic model 3.1. As an example, the state change vector $\Delta\vec{\mathbf{X}}_8 = [-1, 0, 0, 0, 0, 0, 0, 0]^{tr}$ represents the death of an uninfected CD4+ T cell. The state changes (called reactions) for the stochastic model can be differentiated into four categories: cell births (R_i for $i = 1, \ldots, 4$), deaths (R_i for $i = 5, \ldots, 12$), infections (R_i for $i = 13, 14, 15$), and transports through the blood-brain barrier (R_i for $i = 16, \ldots, 19$). There are 19 reactions in all and the rates and state change vectors are given in Table 5. A schematic diagram of the model is present in Figure 24. 500 model simulations for 100 days post-infection were performed using Python 3.5.2, and the Stochpy package. All parameter values are positive and the rates are given in Table 6.

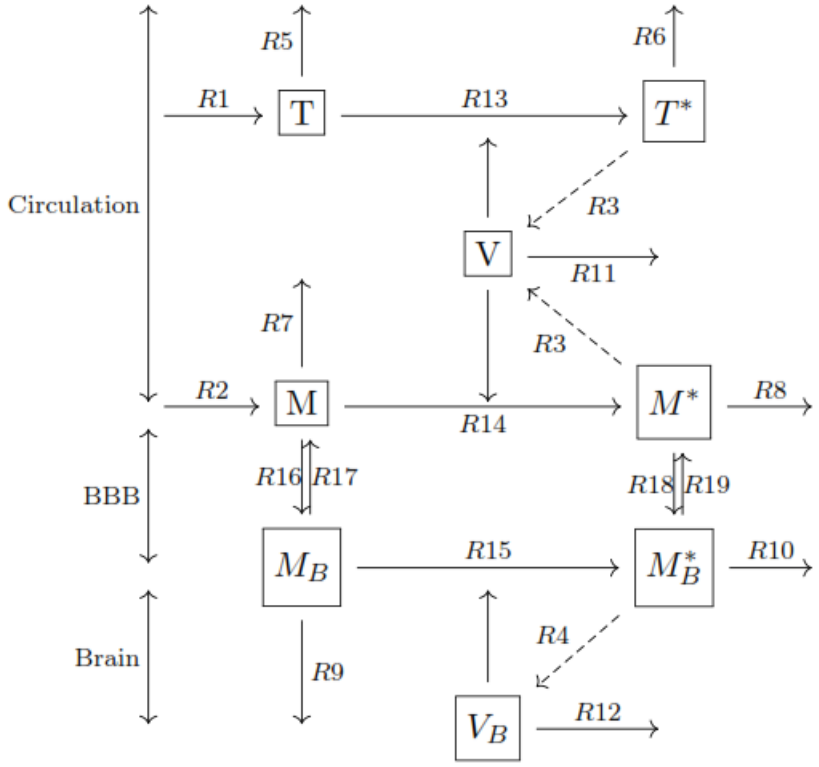

Figure 24: Schematics for the stochastic model.

Results

In the following sections we show the results of 500 numerical simulations for 100 days for each cell type. We first show the computer average trajectories and their respective calculated deterministic predictions. We next examine the average propensity functions for each possible reaction. Finally, we show the average distribution for each cell.

Table 5: Possible state changes during Δt.

Category	R_i	State change vector ($\Delta\vec{\mathbf{X}}_i^{tr}$)	Probability	Description
Births	1	[1,0,0,0,0,0,0,0]	λ	Birth of a CD4+ T cell
	2	[0,0,1,0,0,0,0,0]	λ_M	Birth of a plasma macrophage
	3	[0,0,0,0,0,0,1,0]	$p + p_M$	Production of a free plasma virion
	4	[0,0,0,0,0,0,0,1]	p_M	Production of a free brain virion
Deaths	5	[-1,0,0,0,0,0,0,0]	d	Uninfected CD4+ T cell
	6	[0,-1,0,0,0,0,0,0]	δ	Infected CD4+ T cell death
	7	[0,0,-1,0,0,0,0,0]	d_M	Uninfected plasma macrophage death
	8	[0,0,0,-1,0,0,0,0]	δ_M	Infected plasma macrophage death
	9	[0,0,0,0,-1,0,0,0]	d_M	Uninfected brain macrophage death
	10	[0,0,0,0,0,-1,0,0]	δ_M	Infected brain macrophage death
	11	[0,0,0,0,0,0,-1,0]	c	Clearance of free plasma virion
	12	[0,0,0,0,0,0,0,-1]	c	Clearance of free brain virion
BBB Infections	13	[-1,1,0,0,0,0,-1,0]	βVT	Infection of a target CD4+ T cell
	14	[0,0,-1,1,0,0,-1,0]	$\beta_M VM$	Infection of a plasma macrophage
	15	[0,0,0,0,-1,1,0,-1]	$\beta V_B M_B$	Infection of a brain macrophage
BBB Transits	16	[0,0,-1,0,1,0,0,0]	φ	Uninfected macrophage transport into the CSF
	17	[0,0,1,0,-1,0,0,0]	ψ	Uninfected macrophage transport into the plasma
	18	[0,0,0,-1,0,1,0,0]	φ	Infected macrophage transport into the CSF
	19	[0,0,0,1,0,-1,0,0]	ψ	Infected macrophage transport into the plasma

Table 6: Parameter values for deterministic model.

Model Values			
Initial Values			
Name	Symbol	Value	Source
Initial uninfected T-cells	T_0	38700	Vaidya *et al.* [73]
Initial infected T-cells	T_0^*	0	Kumar *et al.* [45]
Initial uninfected plasma Macrophages	M_0	1463000	Haney *et al.* [30]
Initial infected plasma Macrophages	M_0^*	0	Kumar *et al.* [45]
Initial uninfected CSF Macrophages	M_{B0}	20000	Haney *et al.* [30]
Initial infected CSF Macrophages	M_{B0}^*	0	Kumar *et al.* [45]
Initial plasma free Virions	V_0	200	Kumar *et al.* [45]
Initial CSF free Virions	V_{B0}	0	Kumar *et al.* [45]
Parameter Values			
Name	Symbol	Value	Source
Death rate for uninfected T-cells	d	0.01 (day^{-1})	Stafford *et al.* [67]
Death rate for uninfected Macrophages	d_M	0.00185 (day^{-1})	Prinz *et al.* [53]
Recruitment rate for T-cells	λ	387 (day^{-1})	Calculated
Recruitment rate for Macrophages	λ_M	2743.55 (day^{-1})	Calculated
Viral production from infected T-cells	p	50000 (day^{-1})	Chen *et al.* [16]
Viral production from infected macrophages	p_M	1000 (day^{-1})	Schwartz *et al.* [60]
Viral clearance rate	c	23 (day^{-1})	Ramratnam *et al.* [54]
T-cell infection rate	β	3.5830E-8 (ml/day)	Estimated
Death rate for infected T-cells	δ	1.4551 (day^{-1})	Estimated
Macrophage infection rate	β_M	8.653E-10 (ml/day)	Estimated
Death rate for infected macrophages	δ_M	0.2060 (day^{-1})	Estimated
Rate of macrophage entry into the brain	φ	0.03876 (day^{-1})	Estimated
Rate of macrophage exit from the brain	ψ	8.9953 (day^{-1})	Estimated

Comparison to deterministic model

In this section we used the stochastic model to compare the solutions from the described deterministic model (3.1). In Figure 25 we present the average trajectories for all eight cell types studied. Error bars of one standard deviation from the mean trajectories are shown and the predicted deterministic model values are superimposed on each graph. We observe that except for the uninfected brain macrophages that each predicted trajectory from the deterministic cell values lies within one standard deviation of the average stochastic simulated trajectories, suggesting the stochastic simulations capture the deterministic model. Hence the proposed stochastic model is valid and reasonable.

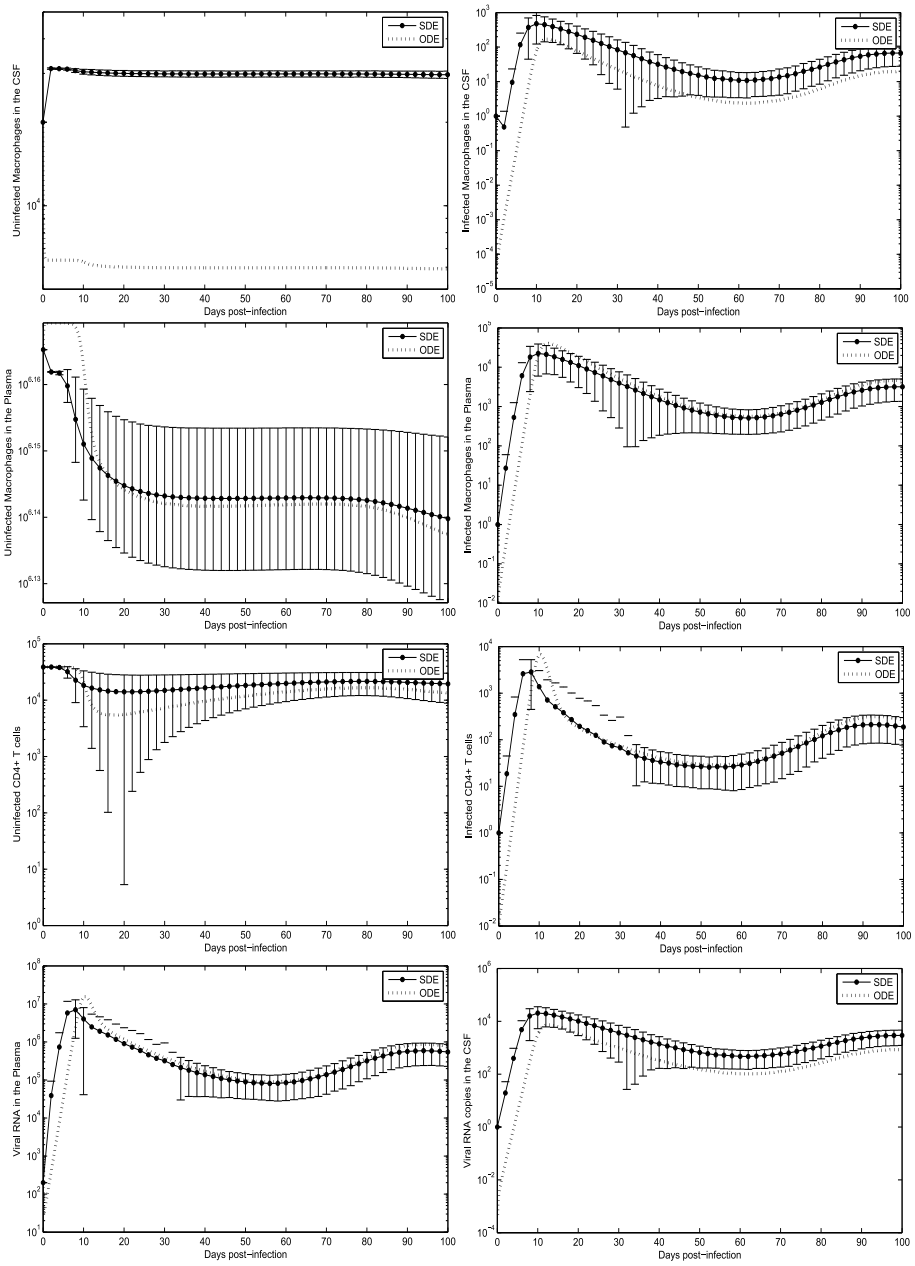

Figure 25: Average trajectories predicted by the stochastic (SDE) model (solid line) compared to the predicted trajectories from the deterministic (ODE) model (dashed line) with error bars of one standard deviation.

In the following subsections, we analyze the calculated average daily propensity values for each reaction. Gillespie [25] defines, for a well-stirred system, the probability that a reaction R_i fires in the next time step, $\mathrm{d}t$, to be $\mathbf{a}_i(\vec{\mathbf{x}})\,\mathrm{d}t$, where $\mathbf{a}_i(\vec{\mathbf{x}})$ is the propensity function. Thus, a propensity function is closely related to the probability of a reaction firing. In the τ-leap stochastic simulation algorithm, a propensity function measures how many reactions will likely occur over a given time interval. It is important to note that a propensity value is not a probability, but as a general rule the higher the propensity value, the likelier that reaction will occur. By analyzing propensity values we can predict when specific reactions, such as new brain macrophage infections, are most likely to fire. Since propensity functions are defined based on cell populations the absolute value of a propensity function is less informative than the day the max value occurs and the length of time a propensity functions remains near a peak value. That is, the shape of a propensity function does not depend on cell populations, thus qualitative results drawn from the shape of a propensity curve provide more information than exact function values.

Infection Reactions

In Figure 26 we plot the mean propensity values at a given time t of the infection reactions (R_i for $i = 5, 6, 7$) from 500 simulations.

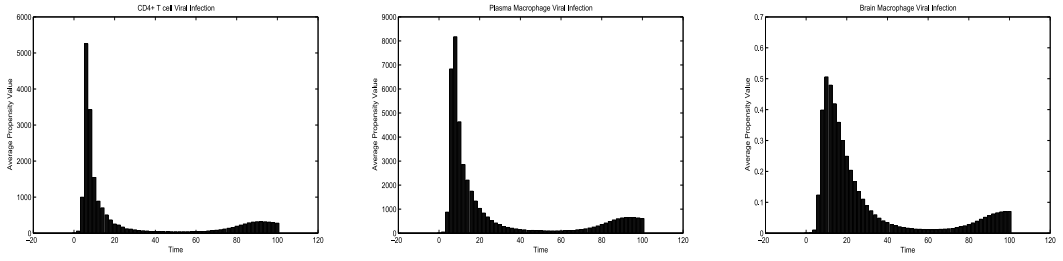

Figure 26: Predicted per day average propensity values for the reactions of CD4+ T cell infections (left), infection of macrophages in the plasma (center), and infection of macrophages in the brain (right).

Each reaction propensity function follows a similar curve, but it is clear that the most likely time for new cell infection is early (~ 2 weeks post-infection), as the propensity functions for the reactions involving new infections peak within the first two weeks. However, it does not appear that a large number of infection reactions are particularly likely outside of the first two weeks, which suggests that new viral infections may not be as high as the first two weeks.

To better understand which infection reactions maintain their highest likelihood longer, we calculated the number of days a reaction's propensity function was within 80% of its peak value and plotted the results in Figure 27. We observe that the infection of plasma cells (T and M) reach their highest likelihoods first before the brain infection reactions become most likely (6-8 dpi vs. 10-14 dpi). This suggests that viral infection in the brain depends on viral infection transporting from the plasma, which is consistent with findings from previous studies [50, 51, 59, 79]. Furthermore we observe that the infection reaction in the brain sustains its high like-

lihood for at least twice as long (4 days vs. 1-2 days) as infection reactions in the plasma. Thus there is a greater window of high infection probability in the brain compared to that in the plasma.

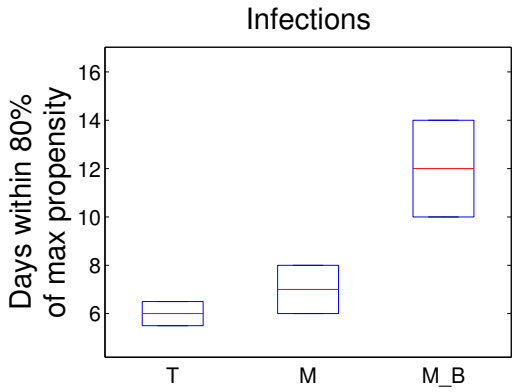

Figure 27: The days in which the reaction propensity functions are within 80% of their max values for infections of uninfected cells.

Viral Production

In this subsection we consider the reaction propensity functions for the production of free virions in the plasma (R_3) and in the brain (R_4). We plot the average propensity functions in Figure 28. We first note that the likelihood of production of free virions in both the brain and the plasma vary considerably depending on time, and in a similar manner as the propensity functions for infections varies. There is a maximum likelihood that occurs during early infection (around the first two weeks). We also note that the plasma viral production reaction has low propensity values for

much of the infection time, whereas the likelihood that free virions are produced in the brain appears for a longer duration.

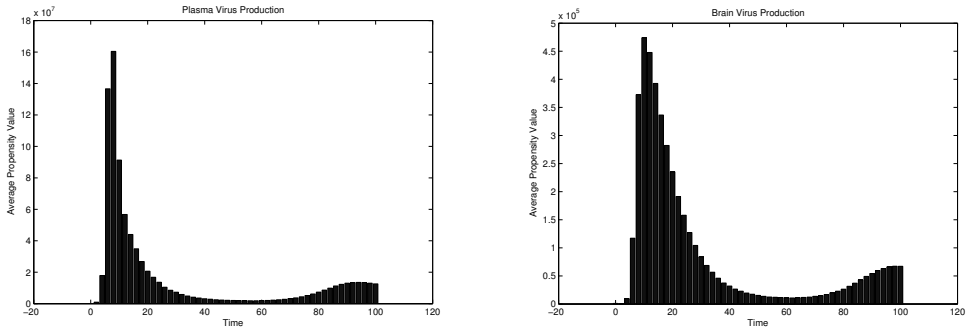

Figure 28: Predicted per day average propensity values for reactions involving production of free virions in the plasma (left) and in the CSF (right).

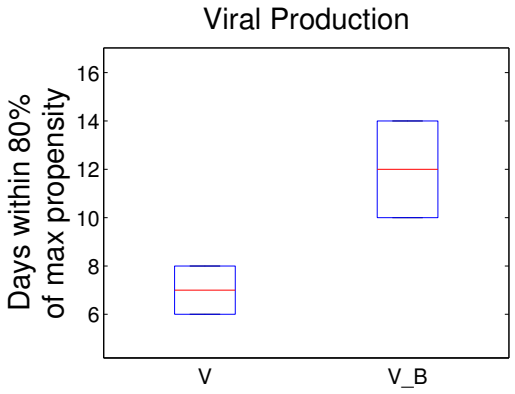

Figure 29: The days in which the reaction propensity functions are within 80% of their max values for the production of free virions in the plasma (V) and in the CSF (V_B).

To analyze this apparent sustained higher probability we plot the number of days that the reactions of viral production in the plasma and the brain maintain at least 80% of their peak propensity values in Figure 29. We observe that the reaction of viral production in the brain reaches its max propensity later (10 dpi vs. 6 dpi) and sustains near-max likelihood longer (4 dpi vs. 2 dpi) than the reaction of viral production in the plasma. This suggests that similar to viral infection reactions, there is a larger time interval for which the virus brain is likely to replicate compared to that in the plasma.

Most Likely Reactions

Although propensity functions are defined based on cell populations, the highest propensity value across the entire set of reactions implies that more firings of

that reaction are likely to occur in a given time interval. Thus we can analyze the most likely reaction at a given time for the entire system. We present the most likely reactions to fire in Table 7 defined by the maximum propensity value at a given time, t. We observe that the highest propensity values revolve around only three reactions: initial transfer of macrophages into the brain, the production of plasma viruses, and the clearance of plasma virions. Specifically, plasma viral clearance becomes more probable a reaction after the first week, but during the seventh week post infection we observe a greater likelihood of viral infection. This is immediately followed by a brief period of more likely viral clearance, and then another month which viral production again is most likely of all reactions. This suggests that most of the cell reactions that occur during infection are the production and clearance of free virions in the plasma. Since there is a significantly higher amount of infected cells producing free virions in the plasma compared to infected cells in the brain, this reaction may be expected.

Table 7: Predicted likeliest reaction to occur at any given time t.

Highest Average Propensity Value	
t in days post-infection	Reaction
0-2	Macrophage transit into the CSF
2-6	Production of plasma free virions
8-52	Clearance of plasma free virions
52-54	Production of plasma free virions
56-58	Clearance of plasma free virions
60-92	Production of plasma free virions
94-100	Clearance of plasma free virions

Average State Distributions

Since propensity functions are strongly related to cell populations, in this section we considered the distributions of cell populations during the days the infection and viral production reactions are most likely to occur. Normal curve fittings to the state probability distributions of infected CD4+ T cells, infected macrophages in the plasma and the brain, and free virions in the plasma and in the brain for 6, 8, and 12 days post-infection are shown in Figure 30. To better analyze these distributions we charted the respective variances of each distribution in Table 8.

We observe that for infected CD4+ T cells there is more stochastic fluctuation (Var $\sim 4 \times 10^5$ vs. Var $\sim 1 \times 10^5$) when T cell infection is likeliest (6 dpi) than afterwards (12 dpi). A similar phenomenon was observed for free virions in the plasma

(Var $\sim 2 \times 10^{12}$ at 6 dpi vs. Var $\sim 7 \times 10^{11}$ at 12 dpi). These findings are consistent with results from stochastic models presented by Allen *et al.* [80].

For infected macrophages we observe that the stochastic variance is greater ($\sim 87\%$ more) during the second week (12 dpi) compared to the first week (6 dpi). This effect is independent of whether the infected macrophages reside in the brain or in the plasma. We note that the free virions in the brain also have a wider distribution (Var $\sim 1.5 \times 10^{7}$ vs. Var $\sim 1.7 \times 10^{6}$) at 12 days post-infection compared to 6 days post-infection. This suggests that the stochastic fluctuation experienced in the brain is primarily related to the infected macrophages. In fact, the days in which the infection reaction propensity functions are near max values correspond to the days that the stochastic fluctuation is greatest for infected cells and free virions.

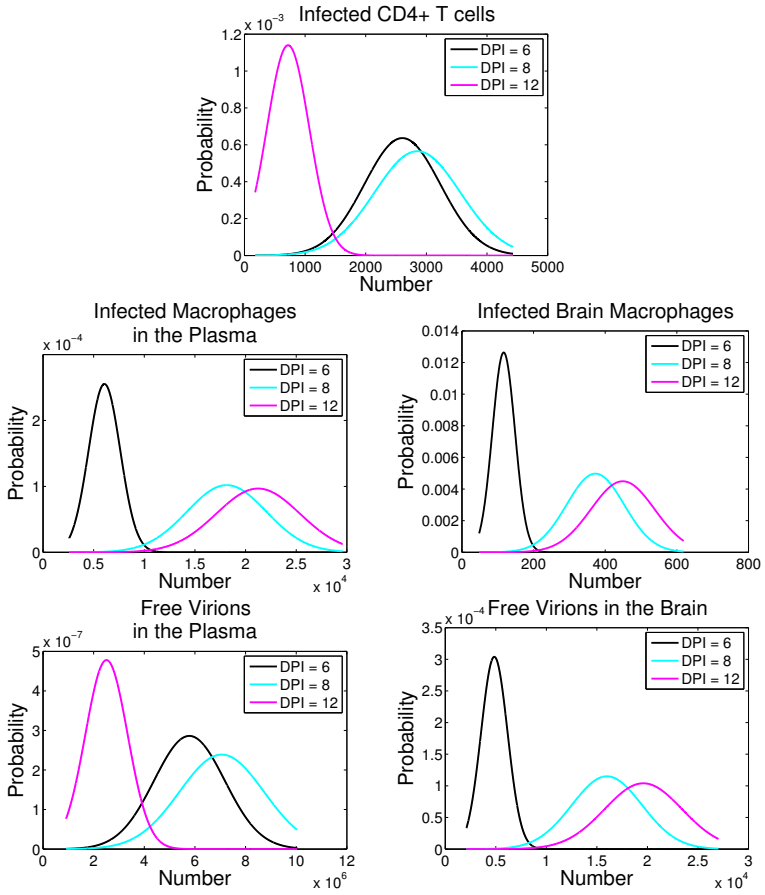

Figure 30: Normal curve fittings to approximate distributions for infected T cells (top row), infected macrophages in the plasma (second row, left column) and in the brain (second row, right column), as well as free virions in the plasma (bottom row, left column) and in the brain (bottom row, right column) for days 6, 8, and 12 post-infection.

Table 8: Table of variances of the state probability distributions for infected cells and free virions on days 6, 8, and 12 post-infection.

Distribution Variances			
Cell Type	6 DPI	8 DPI	12 DPI
T^*	3.9291×10^5	4.98×10^5	1.2248×10^5
M^*	2.440×10^6	1.5325×10^7	1.7015×10^7
M_B^*	996.65	6.43×10^3	7.8889×10^3
V	1.9437×10^{12}	2.7885×10^{12}	6.9649×10^{11}
V_B	1.722×10^6	1.2024×10^7	1.4719×10^7

CHAPTER 6

CONCLUSIONS AND DISCUSSION

HIV-1 remains a major public health challenge and one of the leading causes of death worldwide [4]. While HIV-1 is one of the most studied diseases, viral dynamics in the brain remains one of the least studied aspects of the disease. In particular, the transport of the virus through BBB, the presence of ongoing viral replication in the brain, and the lack of transport of ART drugs through the BBB are poorly understood. In this dissertation, we develop models to address these issues.

The model we developed in chapter 3 can explain the experimental viral load data in the plasma and the CSF from SIV/SHIV infected macaques. Using our model and experimental data we estimated key parameters, including those related to the BBB. In addition, we performed thorough sensitivity analysis, including the one using Latin hypercube sampling technique, to examine the robustness of the dynamics described by our model.

Our model predicts that the entry of HIV virus and/or viral protein via macrophages crossing the BBB is time-varying in nature and the rate of entry may depend on the virus dynamics outside the brain. This shows that while the chronic phase HIV dynamics in the brain may be studied with the brain compartment in isolation as done in some previous studies [56], the modeling study for acute phase HIV-1 dynamics should include both the brain and the plasma as one coupled system. This underscores the importance of getting deeper insights into the BBB and viral

transport across it.

In addition to the virus entering into the brain from outside, our model comparison on the basis of AIC values reveals that there may be ongoing viral replications and production of new virus inside the brain. However, the infection rate of macrophages, the major target cells for viral replication inside the brain, is significantly smaller than that of CD4+ T cells. This implies that macrophages are less susceptible than CD4+ T cells to HIV-1, but once infected, they remain so for a much longer time as indicated by our estimate of a significantly lower death rate of infected macrophages than infected CD4+ T cells. As a result of these infections outside and inside the brain, our model predicts that in the long run the virus in the brain reaches a steady-state nearly three-fold lower than the virus in the plasma. Similarly, there can be a persistence of infected macrophages in the brain with a steady state level significantly lower than the infected cells in the plasma. This indicates that without treatment the virus maintains infectiousness throughout an individual's lifetime not only in the plasma, but also in the brain. This long-term persistence of the virus inside the brain is likely linked to HAND including early-onset dementia and encephalitis [31, 41, 46, 48, 50].

Importantly, our estimates show that the rate of viral exit from the brain, ψ, is significantly higher than the rate of viral entry into the brain, φ. This rate combined with persistent low level ongoing viral replication inside the brain indicates that the brain can be an important reservoir supplying virus into the bloodstream. Since many antiretroviral drug molecules can not enter the brain through the BBB [46], viral replication can continue in the brain despite suppression of virus to undetected levels

in the plasma, thereby causing an obstacle to the cure of HIV through treatment. Upon treatment interruption, the virus produced in the brain may contribute to the further replication outside the brain resulting in the viral rebounds. Therefore, antiretroviral agents that can obstruct the replication inside the brain are necessary for successful control of virus infection.

We also computed the basic reproduction number, $\mathfrak{R}_0$, for each monkey, and found that the value of $\mathfrak{R}_0$ (1.33 to 1.55) is consistent with the previous estimates [74]. Furthermore, we performed a sensitivity analysis to identify the parameters most affecting $\mathfrak{R}_0$. Our results show that those parameters related closely to T cells are the most impactful for determining the value of $\mathfrak{R}_0$, and thus best characterize the initial infection. This suggests that the brain has minimal effect on the initial infectiousness of HIV-1. This result is consistent with the facts that the infection initiates outside the brain first, and it takes some time for the virus to penetrate the BBB and enter the brain [31].

To understand the effects of the blood-brain barrier on the treatment of HIV-1, we extended the basic model (from chapter 3) to the model with treatment terms. In the extended model, we considered two pharmacodynamic terms, namely, the slope of the dose-response curve, and a CPE score. One important finding from the model simulations is that the CPE score plays a significant role on the viral suppression in the brain for drugs with higher slopes ($m > 1.9$), compared to drugs with low slopes ($m < 1.89$). Generally, ART drugs with larger slopes ($m > 1.89$) tend to be protease inhibitors [1] (see Table 4). While our predictions suggest that changing the CPE score does not affect the time that the plasma viral load becomes undetectable

for either drug type, the CPE score of ART can significantly impact the average time for the BVL to reach undetectable levels. In particular, for PIs, a higher CPE score corresponds to a shorter time for the virus to become undetectable in the brain. However, our simulations did not support a relationship between the CPE score and the time to viral undetectability in the brain if ART had a drug with a low slope. A similar phenomena was observed when we included ART with two drugs. Specifically, for two ART drugs with high slopes, the CPE score per drug affected the days to viral undetectability in the CSF, however, if ART included a drug with a low slope and a drug with a high slope, only the CPE score for the drug with a higher slope reduced the days before the BVL became undetectable. In general, for a PI, a higher CPE score implies a higher percentage of a drug that reaches the brain, and thus a lower time to viral undetectability. Hence, our simulations support the results from Letendre [46] for PIs, which illustrates the impact of the BBB on the potential treatment of HIV in the brain.

We further considered the effect the BBB has on drug regimens with higher dose-response curve slopes compared to those with lower slopes. In this case we found that the PVL reached undetectable levels in significantly less time (≈ 50 days vs. ≈ 1 day) if the slope of the dose-response curve of a drug measured over 1.9, independent of the CPE score. This drastic difference in viral reduction time for PIs was not, observed in the BVL. However, for ART with lower slopes the BVL becomes undetectable roughly three weeks before the PVL does, unlike the results from ART with higher slopes. Furthermore, our simulations suggest that the BBB reduces the effect of ART on HIV in the CSF, especially for drugs with higher slopes.

Therefore depending on the slope of the dose-response curves, control of the PVL may not necessarily indicate control of the BVL. For ART protocols with more than two drugs, viral suppression in the plasma also does *not* imply viral suppression in the brain. However, the median days to viral undetectability in the CSF is less if the number of drugs in an ART protocol is higher. Furthermore, for ART regimens with higher drug totals, a measure of the plasma viral load may not accurately reflect the total viral load in the body as viral RNA may still be present in the brain.

The total time viral RNA takes to reach undetectable levels can be quite different depending on the time of treatment initiation. Although early treatment may prevent the establishment of a viral reservoir [8], our model simulations suggest that treatment initiated after 3 dpi, early ART may not always be better. We found that treatment initiated during the second week post-infection (10-14 dpi) may take up to 50% more days on average to reduce viral loads to undetectable levels than ART begun at roughly 9 weeks (60 dpi) post-infection (see Figure 23). Thus, the impact of the BBB may be limited if treatment begins near the ninth week post-infection. Furthermore, initiating treatment during the first few weeks of infection may result in longer periods of high viral loads.

We again computed the viral reproduction number, $\mathfrak{R}_0$ in the present of ART, and observed a dependence of $\mathfrak{R}_0$ on ART effectiveness. It is worth noting that any combination of ART drugs that satisfies $\varepsilon_i + 1.78(\varepsilon_{PIi})^2 \geq 0.14\varepsilon_{PIi} + 0.52$ will prevent infection according to this model.

To explore the stochastic effect on the viral dynamics of HIV1 in the brain we developed a stochastic model and examined the uncertainty that randomness causes

on the viral dynamics of HIV-1 in the brain as well as the plasma. We note that our stochastic model captured the average behavior predicted by the deterministic model. Furthermore, by measuring propensity functions we observed a longer near-peak infection reaction for both viral infection and viral production in the brain compared to those in the plasma, suggesting a longer persistence of viral replication within the brain. This is consistent with findings from several studies [12, 18]. Based on the reaction propensity values we also note that the reaction with the highest likelihood varied between plasma viral production and plasma viral clearance. While results from the deterministic model show a simple decline in virions in the plasma from the peak ($\sim$ 14 dpi) until day 60, our stochastic model suggests that there are a few days in week seven in which infection becomes more likely. While the early viral production reaction suggests early treatment, which supports findings from several studies [8, 17, 75], treatment during the seventh and eighth week may prove beneficial to prevent any re-establishment of peak infection, which supports findings from the model studied in chapter 4.

In order to better understand the stochastic effect of infection, we examined the probability distributions for each infected cells and free virions during peak infection likelihood. The main observation from these distributions was that there are significantly more reactions occurring amid early stages of infection compared with later stages based on distribution variances, which confirms findings from Allen *et al.* [80]. However, outside of peak infection time the stochastic effect is lessened significantly. Furthermore, based off these distribution variances, we observed that viral infection in the plasma is more controlled by CD4+ T cells, and infected macrophages

affect the dynamics in the brain. Thus treatment protocols targeting macrophages may have a greater effect on controlling HIV infection in the brain.

We acknowledge several limitations of this study. We considered only macrophages as targets of HIV-1 inside the brain. However, brain macrophages may differentiate into microglia. Also, small amount of CD4+ T cells may exists within the brain [68] and other cells such as astrocytes may be HIV-1 targets. We did not consider the immune responses, which might be particularly important for the long-term dynamics. We only studied constant treatment, which in turn, often led to viral eradication. In fact, constant treatment is unrealistic. The recent study by Vaidya *et al.* [75] suggests that the pharmacodynamics of each drug play a large role in latent infection. That study also found that the basic reproduction number may not be the most reasonable indicator of infection persistence, suggesting the new threshold called the infection invasion threshold. We did not take into account drug resistance, nor the potential for viral mutation, which could result in viral rebound even amid treatment. Some studies [59, 68] have found that astrocytes and T cells may also transit viral RNA into the brain, but we only considered macrophages in the brain. While these theoretical results offer insight to potential ART treatment improvements, they must be tested by *in vitro* and *in vivo* experiments before any recommendations can be offered in practice. Recent advances have been made in eliminating HIV DNA through CRISPR technology [21], however we considered only viral RNA. Our model does not incorporate mutated virus strands which have been known to evade treatment [77].

Future goals stemming from this dissertation include the need to develop and analyze a model that incorporates a time-varying treatment concentrations to study

the HIV-infection dynamics in the brain as drug concentrations decay. Also, additional work is needed to conduct model analysis and the long-term effects of uncertainty (i.e., global analysis for the stochastic model) discussed in chapter 5. Other areas which could be of interest include: development of a model that can help in understanding the effects of drugs of abuse on HIV-infection dynamics in the brain, analysis of multiple virus types–specifically drug-resistant strands of HIV. Furthermore, we could conduct a study that incorporates both the stochastic uncertainty and time-dependent treatment to extend knowledge on the dynamics of HIV in the brain.

In summary, we developed models to examine the role of the brain and the BBB on the viral dynamics of HIV. Our model predictions suggest that the brain may act as a reservoir of HIV. Furthermore, certain ART drug pharmacodynamic properties may affect the time for the virus to become undetectable. Since infection reactions in the brain maintain their peak likelihoods for longer than infection reactions in the plasma, HIV control strategies that target macrophages that enter the brain may control HIV are recommended.

REFERENCES

1. *Guidelines for the use of antiretroviral agents in adults and adolescents living with hiv*, 2018 (Accessed June 18, 2018), https://aidsinfo.nih.gov/guidelines/html/1/adult-and-adolescent-arv/458/plasma-hiv-1-rna--viral-load--and-cd4-count-monitoring.
2. *United states department of health and human services*, 2019 (Accessed March 12, 2019), https://aidsinfo.nih.gov/understanding-hiv-aids/fact-sheets/19/73/the-hiv-life-cycle.
3. *The seven stages of the hiv life cycle. scientific figure on cronodon*, 2019 (Accessed March 15, 2019), http://cronodon.com/BioTech/Virus_Tech_3.html.
4. *The centers for disease control and prevention*, 2019, (Accessed May 5, 2019), https://www.cdc.gov/hiv/basics/statistics.html.
5. *Application of dental nanomaterials: Potential toxicity to the central nervous system - scientific figure on researchgate*, 2020 (Accessed January 15, 2020), https://www.researchgate.net/figure/fig1_277898937.
6. H Akaike, *A new look at the statistical identification model*, IEEE Transactions on Automatic Control **19** (1974), 716.
7. Edward Allen, *Modeling with itô stochastic differential equations*, vol. 22, Springer Science & Business Media, 2007.
8. Nancie M Archin, Naveen K Vaidya, JoAnn D Kuruc, Abigail L Liberty, Ann Wiegand, Mary F Kearney, Myron S Cohen, John M Coffin, Ronald J Bosch,

Cynthia L Gay, et al., *Immediate antiviral therapy appears to restrict resting cd4+ cell hiv-1 infection without accelerating the decay of latent infection*, Proceedings of the National Academy of Sciences **109** (2012), no. 24, 9523–9528.

9. Venkata Subba Rao Atluri, Melissa Hidalgo, Thangavel Samikkannu, Kesava Rao Venkata Kurapati, Rahul Dev Jayant, Vidya Sagar, and Madhavan PN Nair, *Effect of human immunodeficiency virus on blood-brain barrier integrity and function: an update*, Frontiers in cellular neuroscience **9** (2015), 212.
10. Mohamed G Atta, Sophie De Seigneux, and Gregory M Lucas, *Clinical pharmacology in hiv therapy*, Clinical Journal of the American Society of Nephrology **14** (2019), no. 3, 435–444.
11. Douglas M Bates and Donald G Watts, *Nonlinear regression analysis and its applications*, vol. 2, Wiley New York, 1988.
12. Maria M Bednar, Christa Buckheit Sturdevant, Lauren A Tompkins, Kathryn Twigg Arrildt, Elena Dukhovlinova, Laura P Kincer, and Ronald Swanstrom, *Compartmentalization, viral evolution, and viral latency of hiv in the cns*, Current HIV/AIDS Reports **12** (2015), no. 2, 262–271.
13. C Beguelin, Miriam Vázquez, Manuel Bertschi, S Yerly, Denise de Jong, Klemens Gutbrod, Andri Rauch, and Alexia Cusini, *Viral escape in the central nervous system with multidrug-resistant human immunodeficiency virus-1*, Open forum infectious diseases, vol. 3, Oxford University Press, 2016, p. ofv210.
14. Duncan S Callaway and Alan S Perelson, *Hiv-1 infection and low steady state viral loads*, Bulletin of mathematical biology **64** (2002), no. 1, 29–64.
15. Yang Cao, Daniel T Gillespie, and Linda R Petzold, *Efficient step size selec-*

tion for the tau-leaping simulation method, The Journal of chemical physics **124** (2006), no. 4, 044109.

16. Hannah Yuan Chen, Michele Di Mascio, Alan S Perelson, David D Ho, and Linqi Zhang, *Determination of virus burst size in vivo using a single-cycle siv in rhesus macaques*, Proceedings of the National Academy of Sciences **104** (2007), no. 48, 19079–19084.
17. Tae-Wook Chun, Delphine Engel, M Michelle Berrey, Theresa Shea, Lawrence Corey, and Anthony S Fauci, *Early establishment of a pool of latently infected, resting cd4+ t cells during primary hiv-1 infection*, Proceedings of the National Academy of Sciences **95** (1998), no. 15, 8869–8873.
18. Janice E Clements, Tahar Babas, Joseph L Mankowski, K Suryanarayana, Michael Piatak Jr, Patrick M Tarwater, Jeffrey D Lifson, and M Christine Zink, *The central nervous system as a reservoir for simian immunodeficiency virus (siv): steady-state levels of siv dna in brain from acute through asymptomatic infection*, The Journal of infectious diseases **186** (2002), no. 7, 905–913.
19. Jacky Cresson and Stefanie Sonner, *A note on a derivation method for sde models: Applications in biology and viability criteria*, Stochastic Analysis and Applications **36** (2018), no. 2, 224–239.
20. Nirav Dalal, David Greenhalgh, and Xuerong Mao, *A stochastic model for internal hiv dynamics*, Journal of Mathematical Analysis and Applications **341** (2008), no. 2, 1084–1101.
21. Prasanta K Dash, Rafal Kaminski, Ramona Bella, Hang Su, Saumi Mathews, Taha M Ahooyi, Chen Chen, Pietro Mancuso, Rahsan Sariyer, Pasquale Ferrante,

et al., *Sequential laser art and crispr treatments eliminate hiv-1 in a subset of infected humanized mice*, Nature communications **10** (2019), no. 1, 1–20.

22. Odo Diekmann, JAP Heesterbeek, and Michael G Roberts, *The construction of next-generation matrices for compartmental epidemic models*, Journal of the Royal Society Interface **7** (2010), no. 47, 873–885.
23. Bradley Efron and Robert J Tibshirani, *An introduction to the bootstrap*, CRC press, 1994.
24. Alessandro F Fois and Bruce J Brew, *The potential of the cns as a reservoir for hiv-1 infection: implications for hiv eradication*, Current HIV/AIDS Reports **12** (2015), no. 2, 299–303.
25. Daniel T Gillespie, *Approximate accelerated stochastic simulation of chemically reacting systems*, The Journal of chemical physics **115** (2001), no. 4, 1716–1733.
26. Paul Glendinning, *Stability, instability and chaos: an introduction to the theory of nonlinear differential equations*, vol. 11, Cambridge university press, 1994.
27. Lachlan R Gray, Michael Roche, Jacqueline K Flynn, Steve L Wesselingh, Paul R Gorry, and Melissa J Churchill, *Is the central nervous system a reservoir of hiv-1?*, Current Opinion in HIV and AIDS **9** (2014), no. 6, 552.
28. Shawn J Green, Monte S Meltzer, JB Hibbs, and Carol A Nacy, *Activated macrophages destroy intracellular leishmania major amastigotes by an l-arginine-dependent killing mechanism.*, The Journal of Immunology **144** (1990), no. 1, 278–283.
29. J Hale, *Asymptotic behavior of dissipative systems*, Bull. Am. Math. Soc **22** (1990), 175–183.

30. AF Haney, Joseph J Muscato, and J Brice Weinberg, *Peritoneal fluid cell populations in infertility patients*, Fertility and sterility **35** (1981), no. 6, 696–698.

31. Joanna Hellmuth, Victor Valcour, and Serena Spudich, *Cns reservoirs for hiv: implications for eradication*, Journal of virus eradication **1** (2015), no. 2, 67.

32. Esteban A Hernandez-Vargas and Richard H Middleton, *Modeling the three stages in hiv infection*, Journal of theoretical biology **320** (2013), 33–40.

33. Morris W Hirsch, Hal L Smith, and Xiao-Qiang Zhao, *Chain transitivity, attractivity, and strong repellors for semidynamical systems*, Journal of Dynamics and Differential Equations **13** (2001), no. 1, 107–131.

34. Ying Huang, Chen Zhang, Jianhong Wu, and Jie Lou, *Modelling the hiv persistence through the network of lymphocyte recirculation in vivo*, Infectious Disease Modelling **2** (2017), no. 1, 90–99.

35. Nathan S Ivey, Andrew G MacLean, and Andrew A Lackner, *Acquired immunodeficiency syndrome and the blood-brain barrier*, Journal of neurovirology **15** (2009), no. 2, 111–122.

36. Jiang Ji-Fa, *On the global stability of cooperative systems*, Bulletin of the London Mathematical Society **26** (1994), no. 5, 455–458.

37. Ayumi Kamina, Robert W Makuch, and Hongyu Zhao, *A stochastic modeling of early hiv-1 population dynamics*, Mathematical biosciences **170** (2001), no. 2, 187–198.

38. Tosio Kato, *Perturbation theory for linear operators*, vol. 132, Springer Science & Business Media, 2013.

39. Hwijin Kim and Alan S Perelson, *Dynamic characteristics of hiv-1 reservoirs*,

Current Opinion in HIV and AIDS **1** (2006), no. 2, 152–156.

40. Denise E Kirschner and Alan S Perelson, *A model for the immune system response to hiv: Azt treatment studies*, Tech. report, Los Alamos National Lab., NM (United States), 1993.

41. Scott Koenig, Howard E Gendelman, Jan M Orenstein, Mauro Carlo Dal Canto, Gholam H Pezeshkpour, Margaret Yungbluth, Frank Janotta, Allen Aksamit, Malcolm A Martin, and Anthony S Fauci, *Detection of aids virus in macrophages in brain tissue from aids patients with encephalopathy*, Science **233** (1986), no. 4768, 1089–1093.

42. Herwig Koppensteiner, Ruth Brack-Werner, and Michael Schindler, *Macrophages and their relevance in human immunodeficiency virus type i infection*, Retrovirology **9** (2012), no. 1, 82.

43. Amit Kumar, Wasim Abbas, and Georges Herbein, *Hiv-1 latency in monocytes/macrophages*, Viruses **6** (2014), no. 4, 1837–1860.

44. Rakesh Kumar, Suheydi Orsoni, Lisa Norman, Ashish S Verma, Grissell Tirado, Luis D Giavedoni, Silvija Staprans, Gregory M Miller, Shilpa J Buch, and Anil Kumar, *Chronic morphine exposure causes pronounced virus replication in cerebral compartment and accelerated onset of aids in siv/shiv-infected indian rhesus macaques*, Virology **354** (2006), no. 1, 192–206.

45. Rakesh Kumar, Cynthia Torres, Yasuhiro Yamamura, Idia Rodriguez, Melween Martinez, Silvija Staprans, Robert M Donahoe, Edmundo Kraiselburd, Edward B Stephens, and Anil Kumar, *Modulation by morphine of viral set point in rhesus macaques infected with simian immunodeficiency virus and simian-human*

immunodeficiency virus, Journal of virology **78** (2004), no. 20, 11425–11428.

46. Scott Letendre, *Central nervous system complications in hiv disease: Hiv-associated neurocognitive disorder*, Topics in antiviral medicine **19** (2011), no. 4, 137.

47. Hai Lin and JW Shuai, *A stochastic spatial model of hiv dynamics with an asymmetric battle between the virus and the immune system*, New Journal of Physics **12** (2010), no. 4, 043051.

48. Wolfgang Löscher and Heidrun Potschka, *Drug resistance in brain diseases and the role of drug efflux transporters*, Nature Reviews Neuroscience **6** (2005), no. 8, 591–602.

49. Apoorva Madavilli, *H.i.v. is reported cured in a second patient, a milestone in the global aids epidemic*, 2019 (Accessed March 7, 2019), `https://www.nytimes.com/2019/03/04/health/aids-cure-london-patient.html`.

50. Avindra Nath, *Eradication of human immunodeficiency virus from brain reservoirs*, Journal of neurovirology **21** (2015), no. 3, 227–234.

51. C David Pauza, *Hiv persistence in monocytes leads to pathogenesis and aids1*, Cellular immunology **112** (1988), no. 2, 414–424.

52. John E Pearson, Paul Krapivsky, and Alan S Perelson, *Stochastic theory of early viral infection: continuous versus burst production of virions*, PLoS computational biology **7** (2011), no. 2.

53. Marco Prinz and Josef Priller, *Microglia and brain macrophages in the molecular age: from origin to neuropsychiatric disease*, Nature Reviews Neuroscience **15** (2014), no. 5, 300–312.

54. Bharat Ramratnam, Sebastian Bonhoeffer, James Binley, Arlene Hurley, Linqi Zhang, John E Mittler, Martin Markowitz, John P Moore, Alan S Perelson, and David D Ho, *Rapid production and clearance of hiv-1 and hepatitis c virus assessed by large volume plasma apheresis*, The Lancet **354** (1999), no. 9192, 1782–1785.

55. Ruy M Ribeiro, Li Qin, Leslie L Chavez, Dongfeng Li, Steven G Self, and Alan S Perelson, *Estimation of the initial viral growth rate and basic reproductive number during acute hiv-1 infection*, Journal of virology **84** (2010), no. 12, 6096–6102.

56. Weston C Roda, Michael Y Li, Michael S Akinwumi, Eugene L Asahchop, Benjamin B Gelman, Kenneth W Witwer, and Christopher Power, *Modeling brain lentiviral infections during antiretroviral therapy in aids*, Journal of neurovirology **23** (2017), no. 4, 577–586.

57. Libin Rong and Alan S Perelson, *Modeling hiv persistence, the latent reservoir, and viral blips*, Journal of theoretical biology **260** (2009), no. 2, 308–331.

58. Andrea Saltelli, Marco Ratto, Terry Andres, Francesca Campolongo, Jessica Cariboni, Debora Gatelli, Michaela Saisana, and Stefano Tarantola, *Global sensitivity analysis: the primer*, John Wiley & Sons, 2008.

59. G Schnell, S Joseph, S Spudich, RW Price, and R Swanstrom, *Hiv-1 replication in the central nervous system occurs in two distinct cell types*, PLoS pathogens **7** (2011), no. 10.

60. Elissa J Schwartz, Naveen K Vaidya, Karin S Dorman, Susan Carpenter, and Robert H Mealey, *Dynamics of lentiviral infection in vivo in the absence of adaptive immune responses*, Virology **513** (2018), 108–113.

61. Lin Shen, Ahmad R Peterson, Susan Sedaghat, Moira A McMahon, Marc Callender, Haili Zhang, Yan Zhou, Eleanor Pitt, Karen S Anderson, Edward P Acosta, et al., *Dose-response curve slope sets class-specific limits on inhibitory potential of anti-hiv drugs*, Nature medicine **14** (2008), 762–766.

62. Peter MA Sloot, Sergey V Ivanov, Alexander V Boukhanovsky, David AMC van de Vijver, and Charles AB Boucher, *Stochastic simulation of hiv population dynamics through complex network modelling*, International Journal of Computer Mathematics **85** (2008), no. 8, 1175–1187.

63. Theresa K Smit, Bruce J Brew, Wallace Tourtellotte, Susan Morgello, Benjamin B Gelman, and Nitin K Saksena, *Independent evolution of human immunodeficiency virus (hiv) drug resistance mutations in diverse areas of the brain in hiv-infected patients, with and without dementia, on antiretroviral treatment*, Journal of virology **78** (2004), no. 18, 10133–10148.

64. Hal Smith and Xiao Qiang Zhao, *Robust persistence for semidynamical systems*, Nonlinear Analysis, Theory, Methods and Applications **47** (2001), no. 9, 6169–6179.

65. Hal L Smith, *Monotone dynamical systems: an introduction to the theory of competitive and cooperative systems*, Bulletin (New Series) of the American Mathematical Society **33** (1996), 203–209.

66. Hal L Smith and Paul Waltman, *The theory of the chemostat: dynamics of microbial competition*, vol. 13, Cambridge university press, 1995.

67. Max A Stafford, Lawrence Corey, Yunzhen Cao, Eric S Daar, David D Ho, and Alan S Perelson, *Modeling plasma virus concentration during primary hiv*

infection, Journal of theoretical biology **203** (2000), no. 3, 285–301.

68. Nathalie Strazielle, Rita Creidy, Christophe Malcus, José Boucraut, and Jean-François Ghersi-Egea, *T-lymphocytes traffic into the brain across the blood-csf barrier: evidence using a reconstituted choroid plexus epithelium*, PLoS One **11** (2016), no. 3.
69. Wai-Yuan Tan and Hulin Wu, *Stochastic modeling of the dynamics of cd4+ t-cell infection by hiv and some monte carlo studies*, Mathematical biosciences **147** (1998), no. 2, 173–205.
70. Horst R Thieme, *Convergence results and a poincaré-bendixson trichotomy for asymptotically autonomous differential equations*, Journal of mathematical biology **30** (1992), no. 7, 755–763.
71. ———, *Persistence under relaxed point-dissipativity (with application to an endemic model)*, SIAM Journal on Mathematical Analysis **24** (1993), no. 2, 407–435.
72. Henry C Tuckwell and Emmanuelle Le Corfec, *A stochastic model for early hiv-1 population dynamics*, Journal of Theoretical Biology **195** (1998), no. 4, 451–463.
73. Naveen K Vaidya, Ruy M Ribeiro, Christopher J Miller, and Alan S Perelson, *Viral dynamics during primary simian immunodeficiency virus infection: effect of time-dependent virus infectivity*, Journal of virology **84** (2010), no. 9, 4302–4310.
74. Naveen K Vaidya, Ruy M Ribeiro, Alan S Perelson, and Anil Kumar, *Modeling the effects of morphine on simian immunodeficiency virus dynamics*, PLoS computational biology **12** (2016), no. 9.

75. Naveen K Vaidya and Libin Rong, *Modeling pharmacodynamics on hiv latent infection: choice of drugs is key to successful cure via early therapy*, SIAM Journal on Applied Mathematics **77** (2017), no. 5, 1781–1804.

76. Pauline Van den Driessche and James Watmough, *Reproduction numbers and sub-threshold endemic equilibria for compartmental models of disease transmission*, Mathematical biosciences **180** (2002), no. 1-2, 29–48.

77. M Warren, *Second patient free of hiv after stem-cell therapy*, Nature **567** (2019), 7749.

78. Xiping Wei, Sajal K Ghosh, Maria E Taylor, Victoria A Johnson, Emilio A Emini, Paul Deutsch, Jeffrey D Lifson, Sebastian Bonhoeffer, Martin A Nowak, Beatrice H Hahn, et al., *Viral dynamics in human immunodeficiency virus type 1 infection*, Nature **373** (1995), no. 6510, 117–122.

79. James B Whitney, Alison L Hill, Srisowmya Sanisetty, Pablo Penaloza-MacMaster, Jinyan Liu, Mayuri Shetty, Lily Parenteau, Crystal Cabral, Jennifer Shields, Stephen Blackmore, et al., *Rapid seeding of the viral reservoir prior to siv viraemia in rhesus monkeys*, Nature **512** (2014), no. 7512, 74–77.

80. Y Yuan and LJ Allen, *S.(2011)*, Stochastic models for virus and immune system dynamics. Math. Biosci **234**, no. 2, 84–94.

81. Xiao-Qiang Zhao, *Uniform persistence and periodic coexistence states in infinite-dimensional periodic semiflows with applications*, Canad. Appl. Math. Quart **3** (1995), no. 4, 473–495.

82. Xiao-Qiang Zhao, Jonathan Borwein, and Peter Borwein, *Dynamical systems in population biology*, vol. 16, Springer, 2003.

VITA

Colin T. Barker was born in 1989 in Saint Louis, Missouri. He received a B.A. degree in Mathematics as well as Exercise and Sports Science and minors in Global Studies and Business Administration from Drury University in Springfield, Missouri in 2011. He received a M.S. degree in Mathematics and Statistics from the University of Missouri-Kansas City in 2015. He hopes to continue his research in the future, and teach mathematics to students for as long as he is able.